ELSEVIER

Polymer 42 (2001) 4687–4707

polymer

www.elsevier.nl/locate/polymer

Temperature dependence of the morphology and mechanical properties of poly(vinyl alcohol) drawn films prepared by gelation/crystallization from solutions by X-ray and solid state ^{13}C NMR

M. Matsuo*, Y. Bin, M. Nakano

Department of Textile and Apparel Science, Faculty of Human Life and Environment, Nara Women's University, Nara 630-8263, Japan

Received 26 July 2000; received in revised form 17 October 2000; accepted 15 November 2000

Abstract

The morphology and mechanical properties of PVA were studied using atactic poly(vinyl alcohol) (at-PVA) dry gel films prepared by crystallization from solutions in dimethyl sulfoxide (Me_2SO) and water (H_2O) mixtures, in which Me_2SO/H_2O composition was set to be 60:40. The hot homogenized solution was quenched by pouring it into an aluminum tray controlled at −80°C, thus generating a gel. The crystal lattice modulus along the chain axis was measured by X-ray diffraction. The values were 200–220 GPa, which is independent of temperature up to 170°C. However, the values became lower with further increase in temperature and the value at 200°C became 133 GPa. This tendency is different from the previous reports showing rapid decrease in the crystal modulus at higher temperature than 120°C. The difference means that crystallites within the specimens prepared by quenching the solution ($Me_2SO/H_2O = 60:40$) at −80°C are in much more stable state than those of the previous specimens. In spite of the temperature independence of the crystal modulus along the chain axis and the crystallinity, the storage modulus similar to Young's modulus decreases gradually with increasing temperature. To study the mechanical properties and molecular orientation of the present specimens with the stable crystallites, the orientational behavior of crystallites was estimated in terms of the orientation distribution function of crystallites, and Young's modulus was calculated by using the generalized orientation factors of crystallites and amorphous chain segments estimated from the orientation functions of crystallites and amorphous chain segments. In doing so, the theoretical calculation was carried out by using a three-dimensional model, in which the oriented crystalline layers are surrounded by an anisotropic amorphous phase and the strains of the two phases at the boundary are identical. The theoretical values were in good agreement with the experimental ones. The ^{13}C NMR measurements suggested that the inter-molecular hydrogen bonds may be broken by drawing and the intra-molecular hydrogen bonds are more preferably formed in the *mm* and *mr* sequences with draw ratio but no marked difference in the structure exists between the crystalline and non-crystalline regions, as judged from the hydrogen bonding in the triad sequences. Even so, the spin–lattice relaxation time, T_{1C}, decreased drastically with increasing temperature reflecting drastic activity of chain mobility. Accordingly, the drastic decrease in Young's modulus (the storage modulus) is thought to be due to the fact that chain mobility in the amorphous phase becomes more pronounced as temperature increases.

Keywords: PVA dry gel film; Orientation distribution function; Three-dimensional model

1. Introduction

Since 1974, polymeric fibers and films with high strength and high modulus have been prepared by several methods including gel state spinning [1], ultra-drawing of dried gel films [2–7] and ultra-drawing of single-crystal mats [8,9]. Interesting results have been obtained for polyethylene [2–6] and polypropylene [7]. In particular, Young's modulus of ultra-drawn polyethylene is more than 200 GPa which is close to the crystal lattice modulus in the chain direction measured by X-ray diffraction. The range of application of polyethylene, however, is limited by its low melting point. To improve heat-resistance, ultra-drawing of poly(vinyl alcohol) (PVA) has been carried out as one of the concepts to produce high strength and high modulus materials, since PVA has heat-resistant properties because of a number of intra- and inter-hydrogen bonds. Cha et al., succeeded in producing high modulus PVA fibers by drawing gels prepared by crystallization from semi-dilute solutions in the dimethyl sulfoxide (Me_2SO) and water (H_2O) mixtures [10]. According to their paper, the significant drawability was assured, when the solution with the 60:40 composition was quenched at temperature < -50°C. The resultant tensile strength and Young's modulus of the drawn fiber reached 2.8 and 60 GPa, respectively. Since then, the characteristics

* Corresponding author. Tel.: +81-742-20-3462; fax: +81-742-20-3462.
E-mail address: m-matsuo@cc.nara-wu.ac.jp (M. Matsuo).

0032-3861/01/$ - see front matter
PII: S0032-3861(00)00847-8

of PVA gels and the mechanical properties of the resultant dry gel films have been investigated in terms of the morphology as well as the behavior of PVA molecules in solutions. By using X-ray diffraction, small angle light scattering (SALS) under Hv polarization condition and scanning electron microscopy (SEM), Matsuo et al. pointed out that the mechanical properties of the PVA dry gel films is sensitive to morphology determined by the mixed composition of Me_2SO and H_2O as well as quenching temperature of the solutions and the morphology of the gels and film is maintained to the characteristics of the phase separation of the solutions [11,12]. The formation of optically anisotropic rods within the gel is thought to be due to the liquid–liquid phase separation associated with spinodal decomposition. For example, PVA solutions at elevated temperature are thermodynamically unstable at the gelation temperature and tend to incur phase separation. In such supercooled solutions, compact molecular aggregates may be formed and these connect to the heterogeneous network system (polymer-rich phase). In spite of the ordering of molecules in the polymer-rich phase, the above behavior does not allow the crystallization because of a large amount of solvents. Actually, no appearance of crystallites was confirmed by X-ray diffraction measurements. The ordering structure in the polymer-rich phase, however, forms optically anisotropic rods containing no crystallites, which was confirmed by SALS pattern showing X-type [13]. With the progression of evaporation of solvent, only an indistinct circular pattern was observed indicating random array of quasi-crystallites smaller than the wavelength of the incident beam. The quasi-crystallites within the gels cannot form their crystal lattice as detected by X-ray diffraction. The decrease in solvent content enhanced the progression of crystallization and gels became stiffer. After perfect evaporation of solvents, the resultant PVA film was transparent showing no scattering under Hv polarization condition.

The morphology and mechanical properties of films cast from aqueous or Me_2SO solutions, however, were mainly investigated using commercial fiber and films. The measurements were done to estimate mechanical properties in bulk [14,15], intrinsic properties of PVA such as the crystal lattice modulus along the chain axis, the thermal expansion coefficient along the chain axis [16] and the formation of inter- and intra-molecular hydrogen bonds within the crystallites [14–18]. According to previous works, the crystal lattice modulus as measured by X-ray diffraction decreased with temperature beyond 120°C and the plots of crystal strain along the chain axis against temperature revealed two straight lines with a break point around 120°C [16]. Furthermore, ^{13}C NMR measurements by Horii et al. [17,18], indicated that the significant increase in the fraction of OH groups, free from hydrogen bonds, was confirmed with draw ratio. In spite of a series of refined works [14–18], however, it is very difficult to judge whether the characteristics of commercial PVA films and fibers reported by them reflect the real intrinsic properties of PVA or are attributed to the unstable properties such as dislocation and ordering fluctuation of chains within the crystallites. Incidentally, such unstable properties of the crystallites discussed above have never been observed for ultra-drawn polyethylene films [19].

To avoid such ambiguous properties on measuring intrinsic properties of PVA, this paper deals with the morphology and mechanical properties of high molecular weight PVA films prepared by gelation/crystallization from the semi-dilute solutions in Me_2SO and water H_2O mixtures at −80–20°C. As discussed later, the crystallites prepared by the present method are found to be more stable than those of films cast from aqueous or Me_2SO solutions. Using the present films, theoretical analysis of Young's modulus was carried out on the basis of a two-phase model assuring the homogeneous stress hypothesis for a polycrystalline material by using the generalized orientation factors of crystallites and amorphous chain segments calculated from the orientation functions of crystallites and amorphous chain segments. This mathematical treatment of PVA system is much complicated in comparison with that of polyethylene one. In this theoretical analysis, the orientation of the principal crystallographic axes, the *a*-, *b*-, and *c*-axes, was obtained as an orientation distribution function to facilitate understanding the deformation mechanism. With these methods, further investigation was done to understand the relationship between the morphology and the mechanical properties in terms of crystallinity and molecular chain mobility as a function of temperature.

2. Experimental section

Sample preparation and characterization. PVA powder was used; the sample had polymerization of 17 900 and 98% hydrolysis with the triad tacticity of $mm : mr : rr = 0.23 : 0.50 : 0.27$. By the preliminary experiment, the crystallinity of the high molecular weight PVA sample used in this experiment had slightly higher than those of the lower molecular weight PVA with polymerizations of 2000 and 4000, when the specimens were stretched up to 11 times. The PVA gels were prepared by crystallization from the semi-dilute solutions in the dimethyl sulfoxide (Me_2SO) and water (H_2O) mixtures, the concentration being 10 g/100 ml. The Me_2SO/H_2O composition was set to be 60:40 to assure the greatest significant drawability of PVA films based on a report by Cha et al. [10]. The solutions were prepared by heating the well-blended polymer solvent mixture at 105°C for 40 min. The homogenized solution was poured into an aluminum tray controlled at temperature >100°C and then the tray was placed in a cold bath set at designed temperatures, thus generating a gel. The gels were kept at the quenching temperature for 10 h and then they were immersed in a water bath at 20°C for a week to remove Me_2SO. The gels were dried by evaporating water under ambient conditions. To avoid the uniplanar orientation of

the (101) plane parallel to the film surface by the planer tension during the drying process, specimens with thickness beyond 700 μm were employed, in which the X-ray pattern (end view) exhibited circular diffraction rings, indicating a random orientation of crystallites. The dry gel film with a random orientation of crystallites was cut into strips of length 25 mm and width 10 mm. The strip was clamped in a manual stretching device and placed under nitrogen at 120°C and elongated manually up to 7 times. After stretching, the stretcher with the sample was quenched to room temperature immediately. Further elongation was done slowly at 160°C up to 14 times, to assure stable structure of crystallites with the drawn film. The suitable temperature to realize the facile drawability shifted to higher value as the draw ratio increased. The uniplanar orientation of the (101) plane appeared again even by the elongation of undrawn films with a random orientation of crystallites but this degree was confirmed to be negligible small through end view pattern of X-ray. The density of the films was measured by a pycnometer with *p*-xylene and carbontetrachloride as the medium. The crystallinity was in the range 20–36%. The values were calculated by assuming the densities of crystalline and amorphous (non-crystalline) phases to be 1.345 and 1.268 g/cm^3, respectively [20].

2.1. Experimental procedure

Crystal strain. The crystal lattice strain was observed by a 12-kW rotating anode X-ray generator (Rigaku RDA-rA operated at 200 mA and 40 kV) and monochromatized using a curved graphite monochromator. The incident beam through the monochromator was collimated by a divergent slit with 1/6°. The diffraction beam was passed through a receiving slit of 0.15 mm width and scatter-slit with 1/6° before reaching the counter [5,21]. The intensity peaks from the crystal planes were measured at 0.05° intervals over a time period of 40 s in the desired range of $2\theta_B$ (twice the Bragg angle). The deviation of a peak position was measured as that of the center of gravity of intensity curve with a peak, since it was impossible to detect a very small deviation of the peak directly. The curve for calculating the center of gravity was obtained for the intensity curve for the (002) plane as a function of the twice the Bragg angle from 73 to 77°. Incidentally, the specimen elongation was also found to be negligible small during the measurements of the crystal strain.

Orientation distribution function of the reciprocal lattice vector of crystal planes. Measurements of orientation function of crystal lattice vectors by X-ray diffraction intensity distribution could be performed exactly using a horizontal scanning type goniometer, operating at a fixed time step scan of 0.1°/40 s over a range of twice the Bragg angle $2\theta_B$ from 4 to 50°. By rotating about the film normal direction at 2–5° intervals from 0 to 90°, the intensity distribution was measured as a function of a given rotational angle θ_j, corresponding to the polar angle between the reference axis and the reciprocal lattice vector of the *j*th crystal plane. After several corrections of X-ray diffraction intensity described elsewhere [5,21], the intensity curve was assumed to be due to the contribution of the intensity from the crystalline phase. The intensity curve $I_{cry}(2\theta_B)$ was separated into the contribution from the individual crystal planes, assuming that each peak had a symmetric form given by a Lorenzian function of in Eq. (1), where I_j^o is the maximum intensity of the *j*th peak.

$$I_{cry}(2\theta_B) = \sum_j \frac{I_j^o}{1 + (2\theta_o^j - 2\theta_B)^2/\beta_j^2} \quad (1)$$

Here β_j is the half-width of the *j*th peak at half the peak intensity and θ_o^j is the Bragg angle at which the maximum intensity of the *j*th peak appears. Using the same process at a given θ_j in the range from 0 to 9°, the intensity distribution $I_j(2\theta_j)$ can be determined for the respective *j*th plane after integrating $I_{cry}(2\theta_B)$ by $2\theta_B$ at each θ_j, and consequently the orientation distribution function $2\pi q_j(\cos\theta_j)$ of the *j*th reciprocal lattice vector may be given by

$$2\pi q_j(\cos\theta_j) = \frac{I_j(\theta_j)}{\int_0^{\pi/2} I_j(\theta_j)\sin(\theta_j)\,d\theta_j} \quad (2)$$

The orientation distribution function of crystallites can be calculated on the basis of the orientation functions $2\pi q_j(\cos\theta_j)$ of the reciprocal lattice vectors measured by X-ray diffraction, according to the method proposed by Roe and Krigbaum [22–24].

Melting point. Thermal behavior of dry gels was estimated in terms of melting endotherms of differential scanning calorimetry (DSC) curves. Dry gels, weighing 5 mg, were placed in a standard aluminum sample pan. The samples were heated at a constant rate of 10°C/min.

Mechanical properties. To measure Young's modulus and tensile strength, specimens were elongated at 20°C with an Instron tester at the cross head speed of 5 mm/min. The initial dimensions of the samples were as: length 40 mm; width 4 mm.

The complex dynamic tensile modulus was measured at 10 Hz over the temperature range from −150 to 250°C by using a visco-elastic spectrometer (VES-F) obtained from Iwamoto Machine Co. Ltd. The length of the specimen between the jaws was 40 mm and the width was about 1.5 mm. During measurements, the specimen was subjected to a static tensile strain in order to place the sample in tension during the axial sinusoidal oscillation. The complex dynamic modulus was measured by imposing a small dynamic strain to ensure linear visco-elastic behavior of the specimen [25].

^{13}C NMR measurements. NMR measurements were carried out for dry gel films at room temperature 27–36, 77–82 and 99–104°C with a JEOL, JM-EX270 spectrometer, operating at a static magnetic field of 6.34 T. The values described above correspond to temperature

Table 1
Young's modulus and tensile strength at maximum draw ratio of PVA films prepared by quenching the solutions with 40:60, 50:50, 60:40, 70:30 and 80:20 compositions of mixed solvent at 20, −10, −40 and −80°C

Quenching temperature (°C)	Me_2SO/H_2O composition (vol.%)	Maximum draw ratio (λ)	Birefringence ($\times 10^{-3}$)	Young's modulus (GPa)	Tensile strength (GPa)
20	40:60	10.1	35.5	25.6	0.47
	50:50	10.7	36.2	26.8	0.57
	60:40	11.4	36.8	27.3	0.62
	70:30	11.1	36.6	27	0.63
	80:20	–	–	–	–
−10	40:60	10.3	38.5	27.3	0.52
	50:50	11.3	38.8	30.8	0.62
	60:40	11.5	40.3	32.3	0.71
	70:30	11.4	39.4	31.5	0.67
	80:20	10.3	36.9	31.3	0.61
−40	40:60	10.7	38.8	28.6	0.66
	50:50	12.1	39.4	31.3	0.73
	60:40	12.6	40.5	32.9	0.78
	70:30	12.5	39.8	31.9	0.69
	80:20	10.8	37.4	31.7	0.63
−80	40:60	11.1	39.2	29.2	0.73
	50:50	12.8	40.3	32.3	0.79
	60:40	13.7	40.7	34.5	0.84
	70:30	13.5	40.5	33.5	0.74
	80:20	12.6	39.7	32.1	0.65

fluctuation in a probe during the measurements. A radio frequency of 67.5 MHz was used for detection of ^{13}C resonance. The magic-angle spinning rate was 5–5.5 kHz. The contact time in ^{13}C CP/MAS measurement was 2 ms. The chemical shifts were mainly determined from the higher field signal (29.5 ppm) of adamantane relative to tetramethylsilane (Me_4Si). Spin–lattice relaxation times (T_{1C}) longer than several tens of seconds were estimated using the method developed by Torchia, while T_{1C} shorter than a few seconds was measured by the standard-recovery pulse sequence without CP. A cylinder-type MAS rotor with O-ring seal, the main parts being made of aluminum oxide and zirconia, was used for dry samples to prevent the absorption of moisture by high centrifugal force during the measurements. Incidentally, the contributions from the materials used for the MAS rotor and the probe were removed in determining peak intensity by subtracting spectra obtained by blank measurements from the spectra.

3. Results and discussion

3.1. Morphology and thermal and mechanical properties of PVA films in undrawn and drawn states

Table 1 summarizes birefringence, Young's modulus, tensile strength at the maximum draw ratios of the dry gel films prepared by quenching solutions at the indicated temperatures. The compositions chosen were 40:60, 50:50, 60:40, 70:30 and 80:20. The maximum draw ratio could be realized by the elongation of films prepared by quenching the solution with the 60:40 composition at −80°C. This indicates that the molecular orientation and mechanical properties are strongly affected by the facile drawability, and the greatest drawability can be realized by the control of two factors: the content of Me_2SO in the mixed solvent and quenching temperature of solutions. Incidentally, at the 90:10 and 20:80 compositions, no gelation occurred at 20°C. Of course, Young's modulus and tensile strength of films cast from aqueous or Me_2SO solutions were much lower than those prepared from the 60:40 and 70:30 compositions, because of the unstable structure of crystallites [16–18].

Fig. 1 shows the change of scanning electron micrographs observed for undrawn dry gel films obtained by evaporating mixed solvents with the 60:40 and 70:30 compositions from swollen gels. The gels were prepared by quenching the solutions at desired temperatures. The texture is apparently meshy fibrillar-like interconnected lamellar crystals. The fibrillar texture shows honeycomb-like structure and size of the holes becomes smaller as the quenching temperature decreases. In particular, for the gels prepared by quenching at temperature <-10°C, the morphology seems to be preserved during solvent evaporation at room temperature. No dense network structure, however, was observed for the films cast from aqueous or Me_2SO solutions. This indicates that the dense network structure plays an important role in assuring high drawability, since inner stress within the film is transmitted smoothly in the stretching direction.

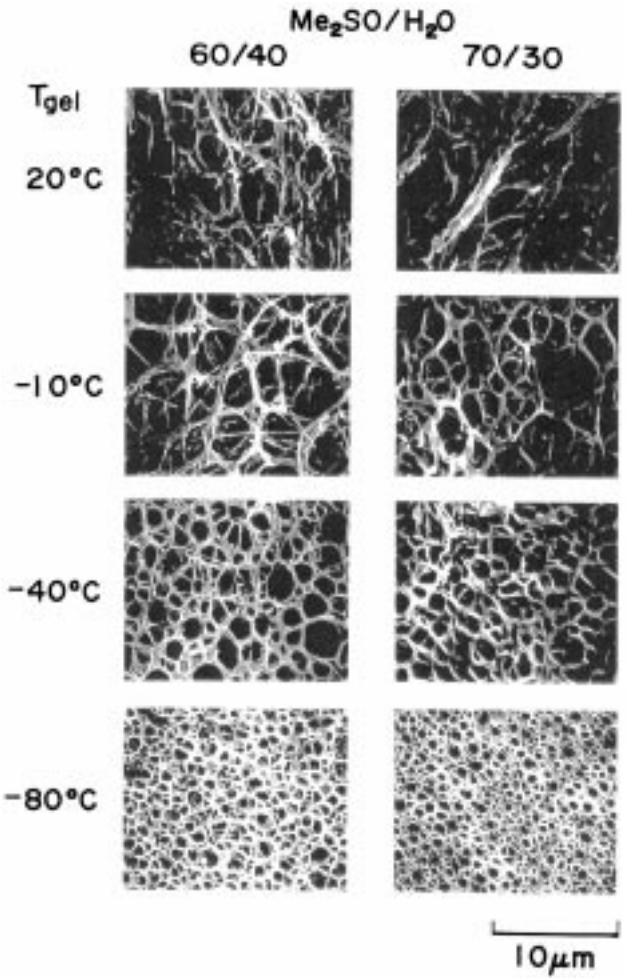

Fig. 1. Scanning electron micrographs of PVA undrawn films prepared by quenching the solutions with 60:40 and 70:30 compositions at the indicated temperature.

Incidentally, no light scattering pattern was observed for the resultant dry gel films under Hv polarization condition indicating that the fibrous tissue with honeycomb-like structure exhibits no optical anisotropy.

Fig. 2 shows the change in the profile of the DSC curves with increasing draw ratio for two kinds of specimens. One is prepared by quenching solutions at 20°C, the other at −80°C. The composition was fixed to be the 60:40. In all cases, the profile shows a single main peak. As can be seen in this figure, the peak position shifts to higher temperature from 233 to 247°C for the specimens prepared by quenching at 20°C and from 242 to 251°C for the specimen prepared by quenching at −80°C, respectively. The detailed observation reveals that the peak profile at −80°C is sharper than that at 20°C. These results indicate that the crystal size at −80°C is bigger than that at 20°C and the fluctuation of chain arrangement and the defects within the crystallites are fewer. Thus the following experiments were carried out by using the specimens which were prepared by quenching the solution with the 60:40 composition at −80°C in order to study the relationship between morphology and mechanical properties. Of course, preliminary DSC experiments offered that for the undrawn and drawn specimens cast from aqueous or Me_2SO solutions, the peak profile is duller and the peak position shifts to lower temperature in comparison with the results in Fig. 2.

3.2. Temperature dependence of crystal lattice modulus and thermal coefficient

Fig. 3 shows the temperature dependence of the crystal lattice modulus measured for the specimens at about $\lambda =$ 13.5. Within an experimental error, the measured values are independent of temperature below 170°C. However, the values become lower with further increase in temperature and the value at 200°C became 133 GPa. This behavior is different from the temperature dependence of polyethylene [19]. According to the report [19], the crystal lattice modulus of polyethylene was maintained at a constant value up to its melting point. Hence, the decrease in the PVA crystal lattice modulus at 170°C is attributed to less perfection of the PVA crystallites in comparison to PE crystallites. Even so, it is evident that the crystallites within the present PVA film are in more stable than those within commercial fibers, since the crystal lattice modulus for commercial fibers tended to decrease at 120°C [16], but that for the present specimen maintained a constant value up to 170°C.

In spite of the temperature independence of the crystal modulus along the chain axis, the storage modulus similar to Young's modulus decreases gradually with increasing temperature as shown in Fig. 4. For the undrawn and drawn films, the storage modulus decreases drastically in the range of −80–40°C and the corresponding loss modulus shows two peaks at −40 and 20°C associated with the local dispersions concerning the motion of side groups and the amorphous dispersion, respectively. The large amorphous dispersion peak at 20°C disappeared above 100°C. Accordingly, the dispersion has been thought to be due to the glass transition. Anyway, the decrease in the modulus of the amorphous phase is thought to be in good correlation with the active mobility of the chain segments. This shall be discussed later in relation to ^{13}C NMR data.

Here it may be noted that the decrease of the crystal lattice modulus above 170°C in Fig. 3 and the decrease in the storage modulus in Fig. 4 must be independent of the large fluctuation of molecular orientation associated with stress relaxation. To demonstrate it, the change in birefringence was measured against temperature. Fig. 5 shows the result. The birefringence shows almost constant value independent of temperature. Generally, the significant transition from crystalline to amorphous phases causes the decrease in birefringence with temperature. However, the decrease in crystallinity with temperature was not observed for the present PVA films, which shall be discussed later. Furthermore, the birefringence for PVA is not sensitive enough to detect small change by the transition because of the small difference between the intrinsic crystal birefringence,

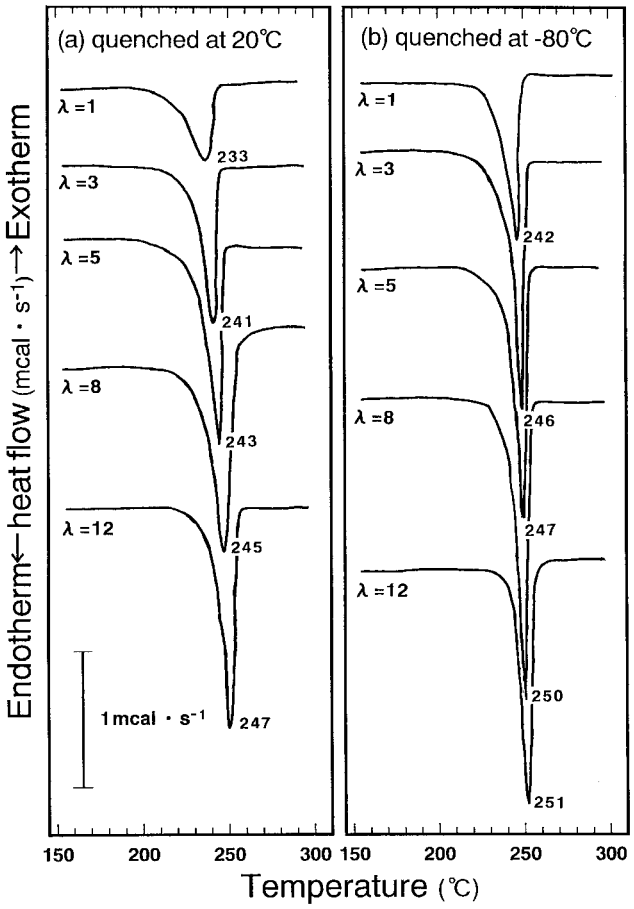

Fig. 2. Change in the DSC curves of PVA films with draw ratio prepared by quenching the solutions with 60:40 composition at 20 and −80°C.

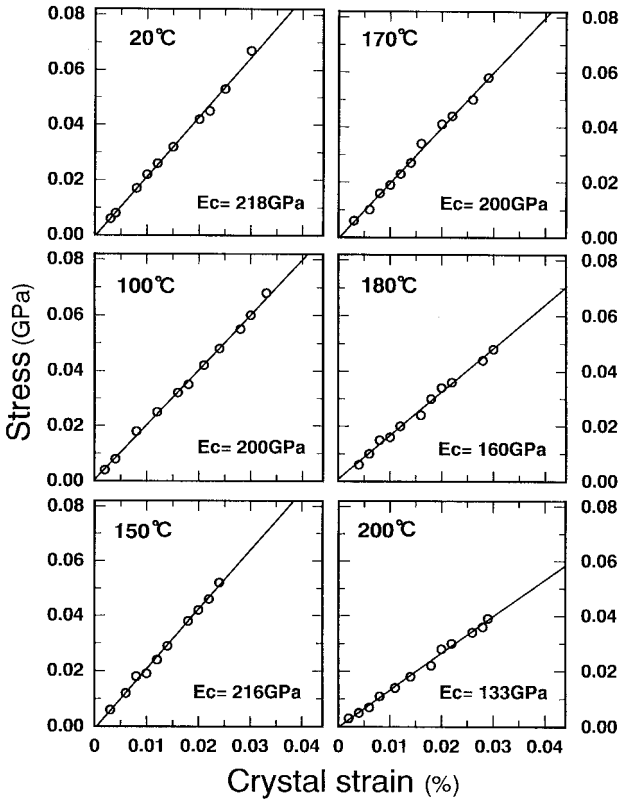

Fig. 3. Change in the crystal lattice modulus of PVA with increasing temperature.

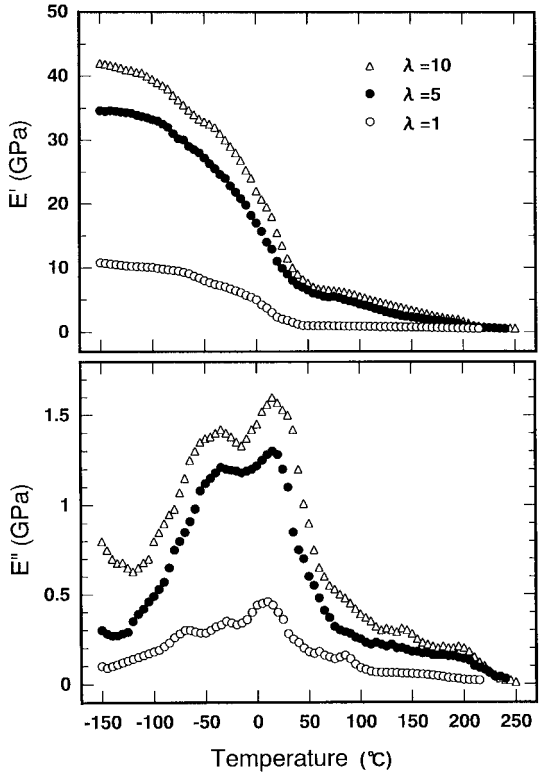

Fig. 4. Temperature dependence of the storage and loss moduli of the PVA with the indicated draw ratio.

0.0443, and amorphous birefringence, 0.0404 [26]. Accordingly, the independence of birefringence in Fig. 5 indicates no orientational change of PVA molecules during the measurements of crystal lattice modulus and Young's modulus as a function of temperature.

Fig. 6 shows the temperature dependence of the crystal strain along the *c*-axis and the corresponding bulk strain in the stretching direction. The measurements were done under the external applied stress listed in this figure. To calculate the thermal expansion coefficients, a strain measured at 27°C was set as the reference. The linear thermal coefficients along the *c*-axis are independent of the applied stress, which satisfy the relationship (see Eqs. (9) and (10)) given in the previous paper [19] and support the validity of the resultant value. The value is $1.97 \times 10^{-5}°C^{-1}$. The bulk coefficient depends on the applied stress and the relationship between the bulk strain and temperature deviates from a straight line with increasing applied stress. Apart from the results in Fig. 6, the deviation from a straight line of the crystal strain was observed for PVA films cast from aqueous or Me_2SO solutions [16]. Such a phenomenon is obviously attributed to the drastic increases in fluctuation of chain arrangement and defects within crystallites.

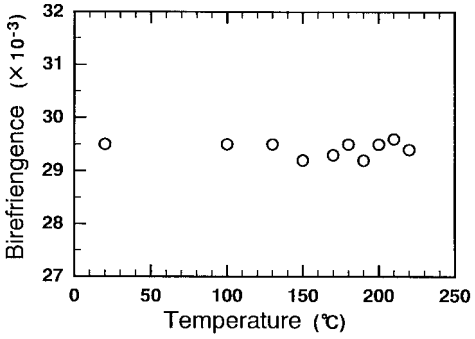

Fig. 5. Change in birefringence of the PVA films at $\lambda = 13.5$.

Orientation distribution function of crystallites. To pursue the detailed relationship between mechanical properties and molecular orientation by using the specimens with stable crystallites, the orientational behavior of crystallites must be estimated in terms of the orientation distribution function of crystallites needed to calculate Young's modulus based on a linear elastic theory. The orientation distribution function of crystallites can be calculated from the orientation distribution functions of the reciprocal lattice vectors of the crystal planes by using a method proposed by Roe and Krigbaum [22–24].

On the basis of the geometrical arrangements shown in Fig. 7, we propose a Cartesian coordinate $0\text{–}U_1U_2U_3$ fixed within a PVA structural unit, with respect to another Cartesian coordinate $0\text{–}X_1X_2X_3$ fixed in a bulk specimen (see Fig. 7(a)). The U_3 axis taken along the c-axis has a random orientation around the X_3 axis along the stretching direction. The orientation of the structural unit within the space of the film specimen may be specified by using three Euler angles, ϕ, θ and η. The angles θ and ϕ, which define the orientation of U_3 axis of the unit within the space, are polar and azimuthal angles, respectively, and η specifies the rotation of the unit around its own U_3 axis. A given jth axis r_j within the unit is specified by the polar angle θ_j and the azimuthal angle ϕ_j with respect to the Cartesian coordinate $0\text{–}X_1X_2X_3$ (see Fig. 7(b)) and specified by polar angle Θ_j and the azimuthal angle Φ_j with respect to the $0\text{–}U_1U_2U_3$ of the unit (see Fig. 7(c)), respectively. More detailed representation is given elsewhere [7,28].

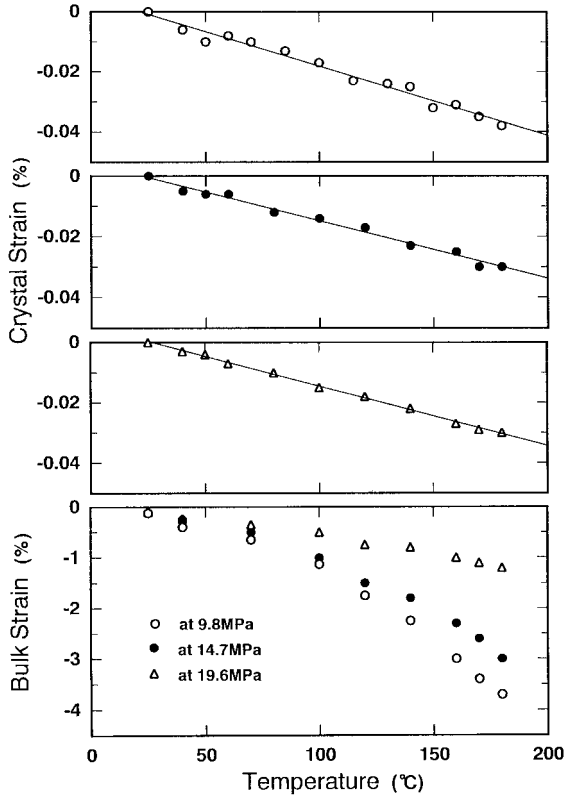

Fig. 6. The relationship between crystal strain along the c-axis and temperature under the indicated stress.

Following Roe and Krigbaum [22–24], the orientation distribution function $\omega(\theta, \eta)$ of crystallites for an uniaxial system around X_3 axis may be calculated from the orientation distribution function of the reciprocal lattice vector of the jth plane, as follows:

$$F^j_{\ell 0} = \langle P_\ell(\cos\theta_j)\rangle = \int_0^{2\pi}\int_0^{\pi} q_j(\cos\theta_j)P_\ell(\cos\theta_j)\sin\theta_j\,\mathrm{d}\theta_j\,\mathrm{d}\phi_j \tag{3}$$

$$F^j_{\ell 0} = F_{\ell 00}P_\ell(\cos\Theta_j) + 2\sum_{n=2}^{\ell}\frac{(\ell-n)!}{(\ell+n)!}\{F_{\ell 0n}\cos n\Phi_j + G_{\ell 0n}\sin n\Phi_j\}P^n_\ell(\cos\Theta_j) \tag{4}$$

$$4\pi^2\omega(\theta,\eta) = \tfrac{1}{2} + \sum_{\ell=2}^{\infty}\left[\frac{(2\ell+1)}{2}\left\{F_{\ell 00}P_\ell(\cos\theta) + 2\sum_{n=2}^{\ell}\frac{(\ell-n)!}{(\ell+n)!}\times(F_{\ell 0n}\cos n\eta + G_{\ell 0n}\sin n\eta)P^n_\ell(\cos\theta)\right\}\right] \tag{5}$$

Here ℓ and n are even integers. $P^n_\ell(x)$ and $P_\ell(x)$ are the associated Legendre polynomials and Legendre polynomials, respectively. $F^j_{\ell 0}$, $F_{\ell 0n}$ and $G_{\ell 0n}$ are the coefficients. $F^j_{\ell 0}$ is the ℓth order orientation factor of the jth crystal plane estimated by X-ray diffraction, while the generalized orientation factors $F_{\ell 0n}$ and $G_{\ell 0n}$ can be determined by solving the linear equations represented by Eq. (4), since there exist more equations than the number of unknown parameters, This procedure was proposed by Roe and Krigbaum [22–24].

In accordance with Roe and Krigbaum, the values of $F_{\ell 0n}$ and $G_{\ell 0n}$ were determined by the least-squares method. To compare the observed $2\pi q_j(\cos\theta_j)$ with those calculated for respective crystal planes, we recalculated $F^j_{\ell 0}$ in turn from $F_{\ell 0n}$ and $G_{\ell 0n}$, which were initially determined by the

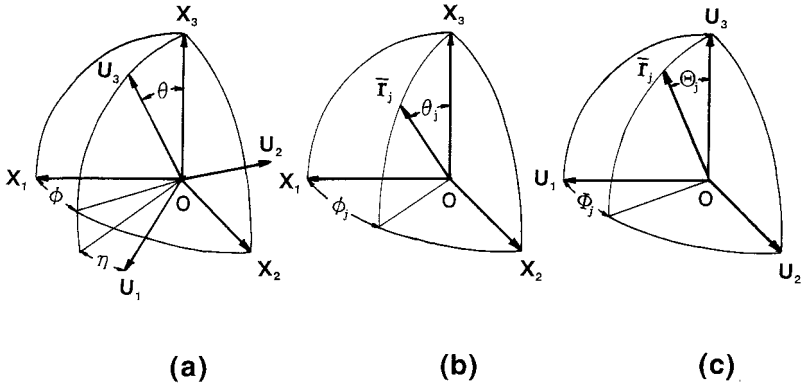

Fig. 7. Cartesian coordinate illustrating the geometrical relation: (a) Euler angles θ and η which specify the orientation of coordinate 0–$U_1U_2U_3$ of structural unit with respect to coordinate 0–$X_1X_2X_3$ of specimen; (b) angles θ_j and ϕ_j which specify the orientation of the given jth axis of the structural unit with respect to the coordinate 0–$X_1X_2X_3$; (c) angles Θ_j and Φ_j which specify the orientation of the jth axis of the structural unit with respect to the coordinate 0–$U_1U_2U_3$.

weighted least-squares method by use of Eq. (4), and further calculated observed $2\pi q_j(\cos\theta_j)$ from the recalculated $F^j_{\ell 0}$ using Eq. (6):

$$2\pi q_j(\cos\theta_j) = \frac{1}{2} + \sum_{\ell=2}^{\infty} \frac{2\ell+1}{2} F^j_{\ell 0} P_\ell(\cos\theta_j) \tag{6}$$

The calculation was continued until the best fit was achieved within the capability of the simplex method [27]. Using the final values of parameters, a mean-square error R between the calculated $F^j_{\ell 0}$ and recalculated $F^j_{\ell 0}$ may be defined as following:

$$R = \frac{\sum_j \sum_\ell \rho_j \{(F^j_{\ell 0})_{\mathrm{cal}} - (F^j_{\ell 0})_{\mathrm{recal}}\}^2}{\sum_j \sum_\ell \rho_j \{(F^j_{\ell 0})_{\mathrm{cal}}\}^2} \tag{7}$$

where ρ_j is weighting factors required in the least-squares calculation. As a first approximation, the initial values of ρ_j were assumed to be proportional to a square of the structure factor and were subsequently modified to obtain the best fit between experimental and calculated results through numerical calculation by computer [27]. The introduction of ρ_j is due to the fact that $2\pi q_j(\cos\theta_j)$ of the crystal plane with high diffraction intensity provides high accuracy but $2\pi q_j(\cos\theta_j)$ of less accurately measured crystal planes contains large experimental error. For example, the value of ρ_j to determine $F_{\ell 0n}$ and $G_{\ell 0n}$ becomes larger for crystal planes with higher diffraction intensity. The values of R in Eq. (7) were 9.1% at $\lambda = 2$, and 9.7% at $\lambda = 5$.

Figs. 8 and 9 compare the observed orientation distribution functions $2\pi q_j(\cos\theta_j)$ with those recalculated for the respective crystal planes for the films with $\lambda = 2$ and 5, respectively. Fairly good agreement between the observed and calculated distribution functions of the reciprocal lattice vectors of the indicated crystal planes was obtained, even for less accurately measured crystal planes with lower weighting factors. Among the (hk0) planes in Fig. 8, the functions $2\pi q_j(\cos\theta_j)$ of the (110), (1$\bar{1}$0) and (2$\bar{1}$0) planes have a sharp peak at 90°, while the functions of the (200) and (020) planes have a peak around 63°. On the other hand, $2\pi q_j(\cos\theta_j)$ concerning the (101) and ($\bar{1}$11) planes having a

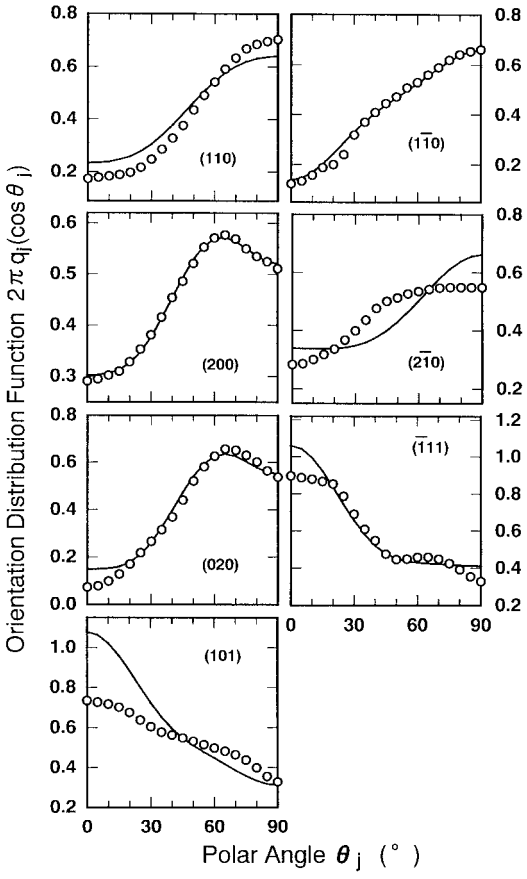

Fig. 8. Orientation distribution functions $2\pi q_j(\cos\theta_j)$ of the reciprocal lattice vectors of the indicated crystal planes of PVA film with a draw ratio of 2. Circles, values of $2\pi q_j(\cos\theta_j)$ obtained from experimental measurements. Solid curves, calculated with the 6-term series.

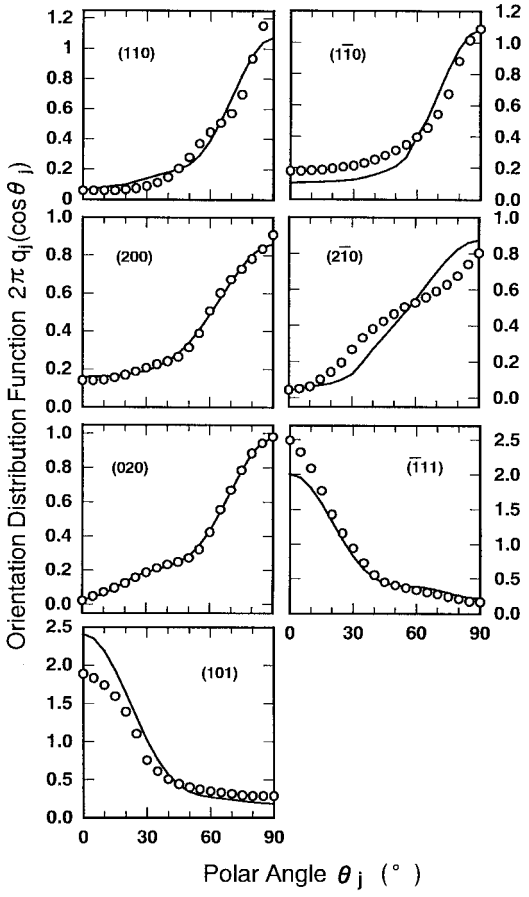

Fig. 9. Orientation distribution functions $2\pi q_j(\cos\theta_j)$ of the reciprocal lattice vectors of the indicated crystal planes of PVA film with a draw ratio of 5. Circles, values of $2\pi q_j(\cos\theta_j)$ obtained from experimental measurements. Solid curves, calculated with the 6-term series.

clearer peak at 0° show very indistinct two shoulders at 20 and 66°, respectively. This behavior indicates that the orientation of crystallites is out of the framework of a floating model assuring a random orientation of crystallites around its own *c*-axis taking an affine orientation. If the orientation of crystallites followed the floating model, all $2\pi q_j(\cos\theta_j)$ for the (*hk*0) planes must show the same monotonous increasing curve with a maximum peak at 90°. Such deviation from the floating model has been observed for polyethylene [29–31] associated with the deformation mechanism of superstructure-like spherulites. However, every $2\pi q_j(\cos\theta_j)$ of the (*hk*0) plane in Fig. 9 shows the similar profile with a maximum at 90°, where $2\pi q_j(\cos\theta_j)$ concerning the (101) and ($\bar{1}$11) planes have different peak magnitude at 0°. Comparing the results in Figs. 8 and 9, the function of each crystal plane becomes sharper indicating the further orientation of crystallites with increasing draw ratio from 2- to 5-fold. To obtain more detailed information, the orientation distribution functions of crystallites are proposed.

Fig. 10(a) and (b) show the orientation distribution functions of crystallites, $\omega(\theta, \eta)$, for the PVA films with $\lambda = 2$ and 5, respectively. Because of a monoclinic form of PVA crystal unit, the map is symmetric at η and $\pi + \eta$. Two maps (a) and (b) are quite different, although they have a common highly populated region at $\theta = 0°$. In addition to the peak at 0°, map (a) shows three highly populated regions. The two peaks at $\theta = 59°$ appeared at $\eta = 45$ and 118°, respectively, and another peak appeared at $\theta = 42°$, $\eta = 170°$. Such considerable η dependence is due to the specific rotation of crystallites around the *c*-axes. This is probably thought to be due to the rotation of crystal lamellae, which shall be discussed later. In map (b), there exist two peaks at $\theta = 0°$ and at $\theta = 65°$, $\eta = 140°$, respectively. The latter peak is not artifact due to the expansion of the

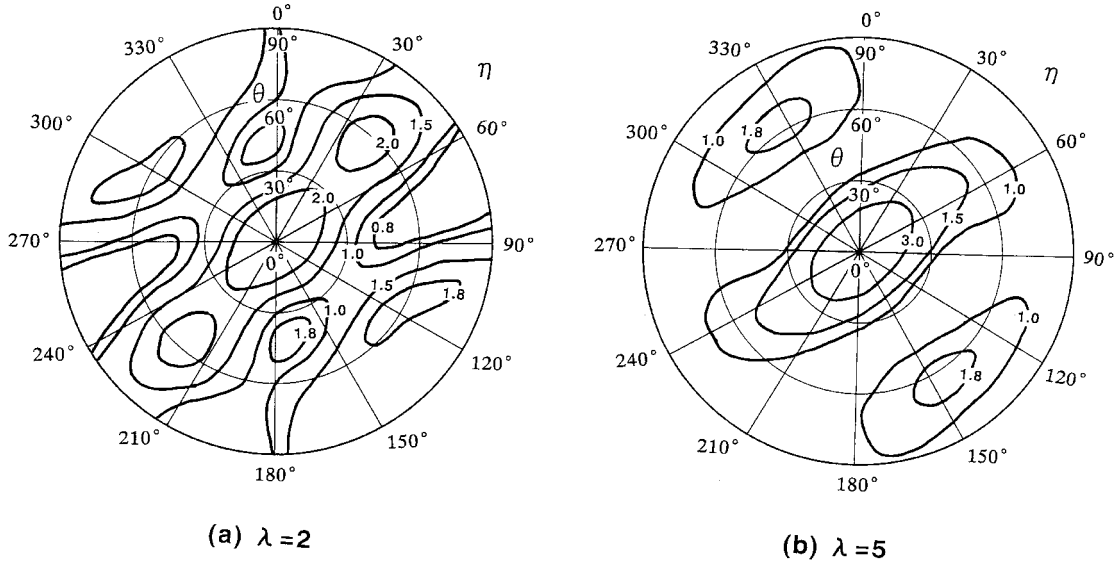

Fig. 10. Orientation distribution functions of crystallites $4\pi^2\omega(\theta, \eta)$ calculated by Eqs. (3)–(5). (a) A drawn film with $\lambda = 2$; (b) A drawn film with $\lambda = 5$.

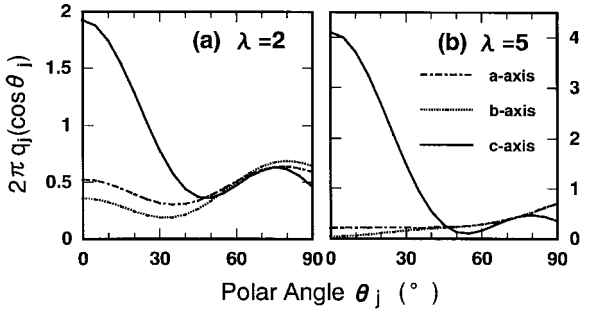

Fig. 11. Orientation distribution functions $2\pi q_j(\cos\theta_j)$ of the *a*-, *b*- and *c*-axes. (a) $\lambda = 2$; (b) $\lambda = 5$.

sharp experimental function of $2\pi q_j(\cos\theta_j)$ into infinite series of spherical harmonics. The η dependence indicates that the orientation of crystallites does not follow a floating model. If all $2\pi q_j(\cos\theta_j)$ of the ($hk0$) planes showed the same curve, $\omega(\theta, \eta)$ provides a circular contour map having a maximum peak at $\theta = 0°$ indicating a random rotation of crystallites around the *c*-axis.

Judging from the observed orientation function of the *j*th crystal plane, it is of interest to consider the orientational behavior of the principle crystallographic axes, *a*-, *b*-, and *c*-axes. To pursue this concept, $F^j_{\ell 0}$ for the *a*-, *b*-, and *c*-axes must be known. They can be calculated from the orientation distribution function of crystallites $\omega(\theta, \eta)$.

The orientation distribution function of the *a*-, *b*-, and *c*-axes can be determined by substituting the values of Θ_j and Θ_j for each axis into Eq. (4) and then by using Eq. (6). Fig. 11(a) and (b) show the results at $\lambda = 2$ and 5, respectively. The orientation functions of the *c*-axis at $\lambda = 2$ and 5 do not show a monotonous decreasing curve indicating the deviation from the floating model. The orientation function at $\lambda = 2$ shows a large peaks at $\theta_j = 0°$ and small peak at 60°. The functions of the *a*- and *b*-axes also have two broad peaks at 0 and 61° indicating the two orientational modes of crystallites. For the *c*-axes, the appearance of the peak at $\theta_j = 62°$ is related to the peaks at $\theta = 59°$, $\eta = 45°$ and at $\theta = 59°$, $\eta = 118°$ in $\omega(\theta, \eta)$ shown in Fig. 10(a), since the orientation of the *c*-axes is given as the integration of $\omega(\theta, \eta)$ by η. At $\lambda = 5$, the orientation function of *c*-axis shows a very large peaks at $\theta_j = 0°$ and a very small peak at 62°, while the functions of the *a*- and *b*-axes show monotonous increasing curves. This indicates the predominance of the random rotation of crystallites around their own *c*-axis with increasing draw ratio. The small peak at 62° is not artifact but trace of the complicated behavior of crystallites at initial elongation shown in Fig. 11(a). The orientation concerning the *a*-, *b*-, and *c*-axes provides one of the important clues to know the detailed information of orientation behavior with regard to crystallites and this information cannot be absolutely derived from the simple evaluation by the second-order orientation factors as has been generally estimated.

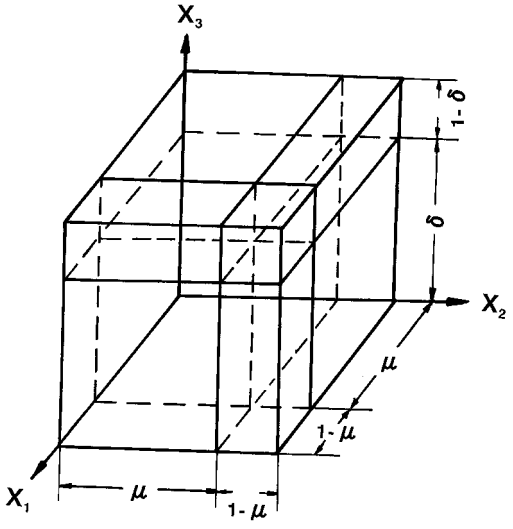

Fig. 12. A composite model in which oriented crystallites are surrounded by an anisotropic amorphous phase.

In order to estimate the orientation behavior of crystallites within the dry gel films, the second-order orientation factor of the amorphous (non-crystalline) chain segments was obtained from the birefringence as estimated by subtraction of the crystalline contribution from the total birefringence, assuming simple additivity. The procedure for evaluating the intrinsic birefringence of crystalline and amorphous phases is described elsewhere [26].

For the film with $\lambda = 2$, F_{200} for the crystallites and F^{am}_{200} for the amorphous chain segments are 0.183 and 0.190, respectively, while for the film with $\lambda = 5$, F_{200} and F^{am}_{200} are 0.450 and 0.463, respectively. The orientational degree of the amorphous chain segments is slightly higher than that of the *c*-axes. This indicates that the preferential orientation of the *c*-axes in the stretching direction is due to straining tie molecules. The complicated orientational behavior of crystallites is thought to be due to the rotation of small crystal lamellae and the orientation of crystallites within the lamellae. Unfortunately, it was very difficult to judge whether this process accompanies the crystal transformation from a folded to a fibrous type at $\lambda = 5$. Small angle X-ray scattering intensity showed a monotonous curve with no scattering peak, when X-ray beam was directed parallel or perpendicular to the film surface.

3.3. Young's modulus of films estimated from crystal and amorphous orientation functions

As discussed in previous papers [32,33], Young's modulus can be calculated by using the generalized orientation factors $F_{\ell 0n}$ and $G_{\ell 0n}$ on the basis of a two-phase model assuming the homogeneous stress hypothesis for a polycrystalline material [34]. The treatment representing as a continuous body is especially suitable for the stretching film, because of no Hv scattering pattern from the aggregation of crystallites such as spherulites and rod-like textures.

Fig. 12 shows a model to satisfy the above concept. The proposed model includes polymeric systems with a low degree of molecular orientation and low crystallinity, in which the oriented crystalline layers are surrounded by an anisotropic amorphous (non-crystalline) phase. Assuming that crystal unit is set in this field, the crystal strains can be represented as a function of composite mode and molecular orientation. This means that the oriented crystallites are surrounded by an anisotropic amorphous phase where molecular chain segments are oriented predominantly in the stretching direction. This model system satisfies the morphological characteristics of a specimen with low crystallinity. Volume crystallinity X_c is represented by $\delta\mu^2$ by the use of the fraction lengths δ and μ in the directions of X_3 and X_2 (and X_1) axes. The crystalline phase given by $\delta\mu^2$ is representative of the aggregation of crystal domains with each characteristic orientation dispersed within oriented amorphous phase, in which average orientation of domains can be given as an orientation distribution function. Of course, this model has problem, since important factors to determine mechanical property such as crystal size, crystal shape and the distance between crystal domains are neglected. At present, however, there is no way to estimate theoretical Young's modulus in the oriented polymeric system. In this model system, amorphous layers are adjacent to the oriented crystalline layers with the interfaces perpendicular to the X_1, X_2 and X_3 axes. Strains of the two phases at the boundary are assumed to be identical. This model can be constructed by following three processes. First, an anisotropic amorphous layer lies adjacent to the crystallite with the interface perpendicular to the X_3 axes and the resultant system is termed as phase I. Secondly, an anisotropic amorphous layer with fraction length $1-\mu$ is attached to the structure of phase I in a plane normal to the X_1 direction to construct phase II. The final phase III can be constructed by adding an anisotropic amorphous layer with fraction length $1-\mu$ to phase II. This procedure was represented elsewhere in detail [14,32,33,35]. For uniaxially stretched films, this model corresponds to a series model at $\mu = 1$, while it corresponds to a parallel model at $\delta = 1$. To shorten this paper, complicated mathematical derivation was eliminated.

In accordance with the mathematical procedure of the generalized Hook's law, Young's modulus in the stretching direction (the X_3 direction) can be given by

$$E = S_{33}^{\mathrm{II}} + \frac{(S_{13}^{\mathrm{II}})^2(S_{33}^{\mathrm{av}} - S_{33}^{\mathrm{II}})}{\left(S_{13}^{\mathrm{II}} + \dfrac{\mu S_{13}^{\mathrm{av}}}{1-\mu}\right)S_{13}^{\mathrm{av}} - \left(S_{11}^{\mathrm{II}} + \dfrac{\mu S_{11}^{\mathrm{av}}}{1-\mu}\right)S_{33}^{\mathrm{av}}} \quad (8)$$

In Eq. (8), S_{ij}^{II} is given as a function of S_{ij}^{I}, S_{ij}^{av} and μ, and S_{ij}^{I} is also given as a function of S_{ij}^{cv}, S_{ij}^{av} and δ in which S_{ij}^{cv} and S_{ij}^{av} are the average compliance of crystal the amorphous phases, respectively. The complicated relationship was represented elsewhere [14,32,33,35].

The relation between the intrinsic compliance of the structural unit and their average compliance is given by

$$S_{ijk\ell}^{\mathrm{cv}} = \sum_{r=1}^{3}\sum_{q=1}^{3}\sum_{p=1}^{3}\sum_{o=1}^{3}\langle a_{io}a_{jp}a_{kq}a_{\ell r}\rangle_{\mathrm{cv}} S_{opqr}^{\mathrm{co}} \quad (9)$$

$$S_{ijk\ell}^{\mathrm{av}} = \sum_{r=1}^{3}\sum_{q=1}^{3}\sum_{p=1}^{3}\sum_{o=1}^{3}\langle a_{io}a_{jp}a_{kq}a_{\ell r}\rangle_{\mathrm{av}} S_{opqr}^{\mathrm{ao}} \quad (10)$$

where $S_{ijk\ell}^{\mathrm{cv}}$ and $S_{ijk\ell}^{\mathrm{av}}$ are average compliance of the crystal and amorphous phases, respectively, and S_{opqr}^{co} and S_{opqr}^{ao} are their intrinsic compliance. $S_{ijk\ell}^{\mathrm{cv}}$ and $S_{ijk\ell}^{\mathrm{av}}$ represented as a tensor quantity can be given as simple relation of S_{ij}^{cv} and S_{ij}^{av}, which are shown in the previous paper [36]. a_{io} is, for example, the direction cosine of the U_o axis with respect to the X_i axis, which is given from the geometrical arrangements elsewhere [36].

Average values of the crystal phase in Eq. (9), $\langle a_{io}a_{jp}a_{kq}a_{\ell r}\rangle_{\mathrm{cv}}$, is given by

$$\langle a_{io}a_{jp}a_{kq}a_{\ell r}\rangle_{\mathrm{cv}} = \int_0^{2\pi}\int_0^{2\pi}\int_0^{\pi}\omega(\theta,\eta)a_{io}a_{jp}a_{kq}a_{lr}\sin\theta\,\mathrm{d}\theta\,\mathrm{d}\phi\,\mathrm{d}\eta \quad (11)$$

where $\omega(\theta,\eta)$ are an orientation distribution function of the crystallites with respect to the coordinate of a specimen. On the other hand, average values of the amorphous phase in Eq. (10), $\langle a_{io}a_{jp}a_{kq}a_{\ell r}\rangle_{\mathrm{av}}$, is given by

$$\langle a_{io}a_{jp}a_{kq}a_{\ell r}\rangle_{\mathrm{av}} = \int_0^{2\pi}\int_0^{2\pi}\int_0^{\pi}\omega_{\mathrm{am}}(\theta)a_{io}a_{jp}a_{kq}a_{\ell r}\sin\theta\,\mathrm{d}\theta\,\mathrm{d}\phi\,\mathrm{d}\eta \quad (12)$$

where $\omega_{\mathrm{am}}(\theta)$ is an orientation distribution function of the amorphous chain segments.

When both the structural units have a uniaxial orientation around the X_3 axis (stretching direction), the generalized orientation factors $F_{\ell 0n}$ and $G_{\ell 0n}$ of the crystallites and $F_{\ell 00}^{\mathrm{am}}$ of the amorphous phase can be represented by using $\omega(\theta,\eta)$ and $\omega_{\mathrm{am}}(\theta)$, respectively, as follows:

$$F_{\ell 0n} = \int_0^{2\pi}\int_0^{2\pi}\int_0^{\pi}\omega(\theta,\eta)P_\ell^n(\cos\theta)\cos n\eta\sin\theta\,\mathrm{d}\theta\,\mathrm{d}\phi\,\mathrm{d}\eta \quad (13)$$

$$G_{\ell 0n} = \int_0^{2\pi}\int_0^{2\pi}\int_0^{\pi}\omega(\theta,\eta)P_\ell^n(\cos\theta)\sin n\eta\sin\theta\,\mathrm{d}\theta\,\mathrm{d}\phi\,\mathrm{d}\eta \quad (14)$$

and

$$F_{\ell 0n}^{\mathrm{am}} = \int_0^{2\pi}\int_0^{2\pi}\int_0^{\pi}\omega_{\mathrm{am}}(\theta)P_\ell(\cos\theta)\sin\theta\,\mathrm{d}\theta\,\mathrm{d}\phi\,\mathrm{d}\eta \quad (15)$$

For an orthorhombic crystal form like polyethylene, $G_{\ell 0n} = 0$.Using Eqs. (9)–(15), for example, S_{33}^{cv} of the crystal phase and S_{33}^{av} of the amorphous phase in the stretching

direction may be given by

$$\begin{aligned}
S_{33}^{cv} = {} & \tfrac{1}{8}S_{11}^{co}\left\{\tfrac{1}{105}F_{404} - \tfrac{8}{105}F_{402} + \tfrac{24}{35}F_{400} + \tfrac{8}{7}F_{202}\right. \\
& \left. - \tfrac{16}{7}F_{200} + \tfrac{8}{5}\right\} + \tfrac{1}{8}S_{22}^{co}\left\{\tfrac{1}{105}F_{404} + \tfrac{8}{105}F_{402}\right. \\
& \left. + \tfrac{24}{35}F_{400} - \tfrac{8}{7}F_{202} - \tfrac{16}{7}F_{200} + \tfrac{8}{5}\right\} \\
& + S_{33}^{co}\left\{\tfrac{8}{35}F_{400} + \tfrac{4}{7}F_{200} + \tfrac{1}{5}\right\} - \tfrac{1}{8}(2S_{12}^{co} + S_{66}^{co}) \\
& \times\left\{\tfrac{1}{105}F_{404} - \tfrac{8}{35}F_{400} + \tfrac{16}{21}F_{200} - \tfrac{8}{15}\right\} \\
& + \tfrac{1}{2}(2S_{13}^{co} + S_{55}^{co})\left\{\tfrac{2}{105}F_{402} - \tfrac{8}{35}F_{400} + \tfrac{1}{21}F_{202}\right. \\
& \left. + \tfrac{2}{21}F_{200} + \tfrac{2}{15}\right\} + \tfrac{1}{2}(2S_{23}^{co} + S_{44}^{co})\left\{\tfrac{1}{105}F_{402}\right. \\
& \left. + \tfrac{8}{35}F_{400} + \tfrac{1}{21}F_{202} - \tfrac{2}{21}F_{200} - \tfrac{2}{15}\right\} \\
& - \tfrac{1}{28}S_{16}^{co}\left\{\tfrac{1}{15}G_{404} - \tfrac{4}{15}G_{402} + 4G_{202}\right\} \\
& + \tfrac{1}{28}S_{26}^{co}\left\{\tfrac{1}{15}G_{404} + \tfrac{4}{15}G_{402} - 4G_{202}\right\} \\
& - \tfrac{1}{21}(S_{36}^{co} + S_{45}^{co})\left\{\tfrac{2}{5}G_{402} + G_{202}\right\} \qquad (16)
\end{aligned}$$

and

$$\begin{aligned}
S_{33}^{av} = {} & S_{11}^{av}\left\{\tfrac{3}{35}F_{400}^{am} - \tfrac{2}{7}F_{200}^{am} + \tfrac{1}{5}\right\} \\
& + S_{22}^{av}\left\{\tfrac{3}{35}F_{400}^{am} - \tfrac{2}{7}F_{200}^{am} + \tfrac{1}{5}\right\} \\
& + S_{33}^{av}\left\{\tfrac{8}{35}F_{400}^{am} + \tfrac{4}{7}F_{200}^{am} + \tfrac{1}{5}\right\} + (2S_{12}^{ao} + S_{66}^{am}) \\
& \times\left\{\tfrac{1}{35}F_{400}^{am} + \tfrac{2}{7}F_{200}^{am} - \tfrac{1}{15}\right\} - (2S_{13}^{ao} + S_{55}^{am}) \\
& \times\left\{\tfrac{4}{35}F_{400}^{am} - \tfrac{1}{21}F_{200}^{am} - \tfrac{1}{15}\right\} - (2S_{23}^{ao} + S_{44}^{am}) \\
& \times\left\{\tfrac{4}{35}F_{400}^{am} + \tfrac{1}{21}F_{200}^{am} - \tfrac{1}{15}\right\} \qquad (17)
\end{aligned}$$

where the orientation factors in Eq. (16) may be given by

$$\begin{aligned}
& F_{200} = \tfrac{1}{2}(3\langle\cos^2\theta\rangle - 1) \qquad F_{202} = 3\langle\sin^2\theta\cos 2\eta\rangle \\
& F_{400} = \tfrac{1}{8}(35\langle\cos^4\theta\rangle - 30\langle\cos^2\theta\rangle + 3) \\
& F_{402} = \tfrac{15}{2}\langle(7\cos^2\theta - 1)\sin^2\theta\cos 2\eta\rangle \\
& F_{404} = 105\langle\sin^4\theta\cos 4\eta\rangle \qquad G_{202} = 3\langle\sin^2\theta\sin 2\eta\rangle \\
& G_{402} = \tfrac{1}{8}\langle(7\cos^2\theta - 1)\sin^2\theta\sin 2\eta\rangle \\
& G_{404} = 105\langle\sin^4\theta\sin 4\eta\rangle
\end{aligned} \qquad (18)$$

The representation of Eq. (16) for a PVA crystal unit is much complicated in comparison with that of polyethylene. The problem that now arises has been how the value of the intrinsic compliance S_{uv}^{co} and S_{uv}^{ao} of PVA can be determined theoretically. The values as the pioneering work were obtained by Tashiro et al. [37] by using **B** matrix at absolute temperature and their values are used to carry out the numerical calculation.

The intrinsic elastic compliance S_{uv}^{ao} of the amorphous phase needed in the numerical calculation is not quite certain. In accordance with the previous method [33], however, the values can be estimated as a crude approximation, assuming that the following relation between the potential energy $P(r)$ of Lenard–Jones and the atomic or molecular distance r holds for a non-crystalline chain.

$$P(r) = -\frac{c}{r^n} + \frac{d}{r^m} \qquad (19)$$

where $m = 9 - 12$ and $n = 1$ or 6 for an ionic or molecular crystal, respectively. Then, neglecting the repulsion term in Eq. (19) for r greater than the equilibrium distance, the elastic compliance, S_{11}^{ao} and S_{22}^{ao}, may be estimated by taking the second-order derivative of $P(r)$ [33,38]. Then

$$S_{11}^{ao} = S_{22}^{ao} = \left\{\frac{\rho_c}{\rho_a}\right\}^4 S_{11}^{c'} \qquad (20)$$

where $S_{11}^{c'}$ in Eq. (20) corresponds to S_{11}^{cv} at $\theta = 0°$. ρ_c and ρ_a are the intrinsic densities of the crystalline and amorphous phases. On the other hand, the expansion of the amorphous phase is assumed to occur only along the lateral direction of the polymer chain, not lengthwise. The compliance S_{33}^{ao} may be estimated by assuming that the modulus along the chain axis is proportional to the number of chain molecules in the unit area perpendicular to the chain direction, and the modulus is independent of temperature. Thus we have,

$$S_{33}^{ao} = \left\{\frac{\rho_c}{\rho_a}\right\}S_{33}^{co} \qquad (21)$$

The other compliance is given by Hibi et al. [14]

To calculate the mechanical properties according to the method by Matsuo [33], the fourth-order orientation factor F_{400}^{am} of the amorphous chain segments must be estimated. Unfortunately, this factor cannot be obtained from birefringence measurements and therefore must be calculated by assuming a common function as an orientation function of amorphous chain segments. In this paper, the mean fourth power of direction cosine $\langle\cos^4\theta\rangle_{am}$ was calculated from an inversely superposed Gaussian function given in the previous papers [33].

Fig. 13(a) and (b) show the μ dependence of Young's modulus E calculated at $\nu_{12}^{ao}(= \nu_{13}^{ao}) = 0.33$ and 0.49, respectively. The former and latter value of ν_{12}^{ao} correspond to the mechanical property of the amorphous phase similar to an ideal rubber elasticity and similar to somewhat tougher or glass state, respectively. The numerical calculation was carried out from Eqs. (8)–(21) using the intrinsic crystal elastic compliance S_{uv}^{co} proposed by Tashiro et al. [37]. These calculated values at $\lambda = 2$ and 5 are hardly affected

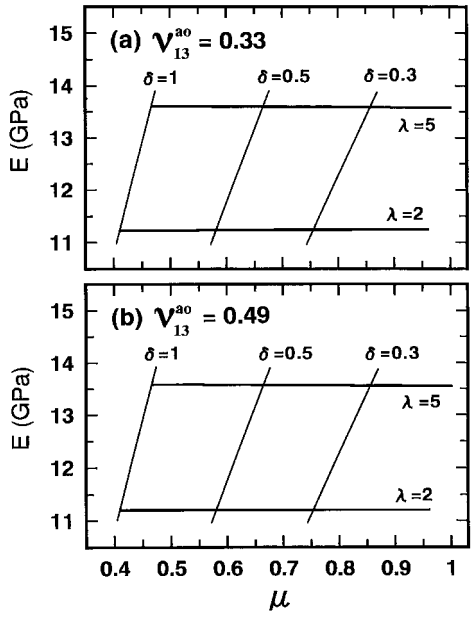

Fig. 13. The μ dependence of Young's modulus calculated in Eqs. (8)–(21): (a) $\upsilon_{12}^{ao} = 0.33$; (b) $\upsilon_{12}^{ao} = 0.49$.

by Poisson's ratio of $\upsilon_{12}^{ao}(= \upsilon_{13}^{ao})$ of the amorphous phases. In this figure, the relationship between δ and μ can be determined by $X_c = \delta\mu^2$. For example, μ is 0.181 at $\delta = 1$ and 0.256 at $\delta = 0.5$ for $\lambda = 5$, while μ is 0.154 at $\delta = 1$ and 0.218 at $\delta = 0.5$ for $\lambda = 2$. E slightly decreases with μ, although this tendency is hard to be recognized in this figure. The calculated results predict that even for two specimens with the same crystallinity and degree of molecular orientation, their Young's moduli slightly differ, depending on the composite mode of the crystalline and amorphous

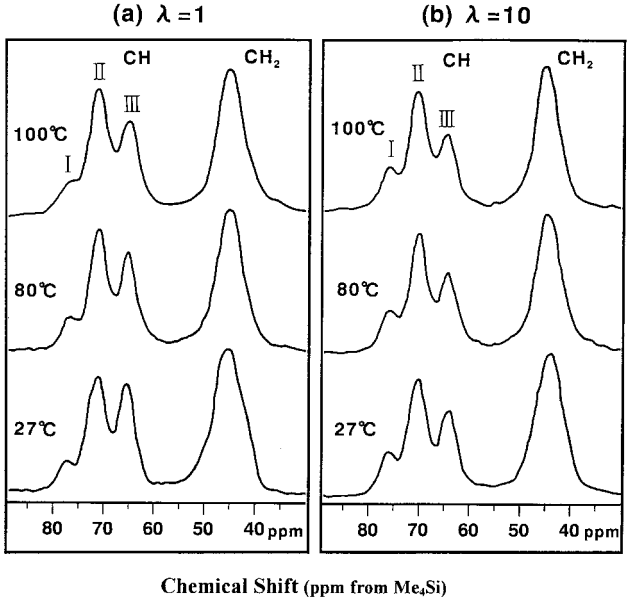

Fig. 14. ^{13}C CP/MAS spectra of PVA films measured at indicated temperature: (a) $\lambda = 1$; (b) $\lambda = 10$.

phases. However, the change is found to be very small to be negligible. As shown in Fig. 13, the calculated values are approximately 11.2 GPa at $\lambda = 2$ and 13.5 GPa at $\lambda = 5$.

It should be noted that all the theoretical Young's moduli calculated using S_{uv}^{co} of Tashiro et al. [37] are in good agreement with the experimental values, 9.1 GPa at $\lambda = 2$ and 13.3 GPa at $\lambda = 5$. In spite of the abnormality between the results measured at room temperature and the theoretical results at absolute temperature, such small difference is due to the fact that no marked difference exists between the structure at room temperature and that at absolute temperature, when PVA films with stable crystallites are used as test specimen. In the numerical calculation, the values of S_{11}^{ao} and S_{33}^{ao} in the present work are given as the intrinsic values of the amorphous phase using Eqs. (20) and (21), although the elastic compliance, S_{11}^{ao} and S_{33}^{ao}, of the amorphous phase depend on the molecular orientational degree of the amorphous chain segments. If the real theoretical values of S_{uv}^{co} and S_{uv}^{ao} at room temperature are proposed by considering harmonic effects, perfect agreement shall be realized.

The relationship between molecular dynamics and mechanical properties in bulk specimens. Fig. 14(a) and (b) show CP/MAS spectra for the PVA films at $\lambda = 1$ and 10 measured at 27–36, 77–82, and 99–104°C. According to the previous works [17,18,39–41], the CH resonance line of each specimen splits into a triplet, I, II and III, which are assigned to central CH carbons I, II and III in *mm*, *mr* and *rr* sequences of the PVA chain with planer zigzag structure. Here, the OH group bonded to the CH carbon I forms intramolecular hydrogen bonds with two OH groups on both sides in the *mm* sequence. On the other hand, the corresponding OH groups associated with CH carbons II and III form one and no inter-molecular hydrogen bonds with the neighboring OH groups in *mr* and *rr* sequences, respectively.

As can be seen in this figure, the relative intensities of lines I, II and III are obviously in disaccord with the fractions of *mm*, *mr* and *rr* sequences with the triad tacticity of $mm : mr : rr = 0.23 : 0.50 : 0.27$. For example, the relative intensity ratio of lines I, II and III apparently deviates from 1:2:1 for at-PVA used in this experiment. In spite of the marked downfield shifts of line I and II, it is evident that all OH groups in the *meso* sequences do not form intramolecular hydrogen bonds and some of them are associated with the inter-molecular hydrogen bonding. Since the intermolecular hydrogen bonding is thought to be independent of any downfield shift, the spectra imply that line I is ascribed purely to the CH carbons associated with the two intramolecular hydrogen bonds in some of the *mm* sequences. However, as pointed by Horii et al. [17,18], additional contributions appear for lines II and III: CH carbons forming one intra-molecular hydrogen bond in the *mm* sequences in addition to those in *mr* sequences for line II and CH carbons associated with no intra-molecular hydrogen bonding in the *mm* and *mr* sequences as well as in the *rr* sequence

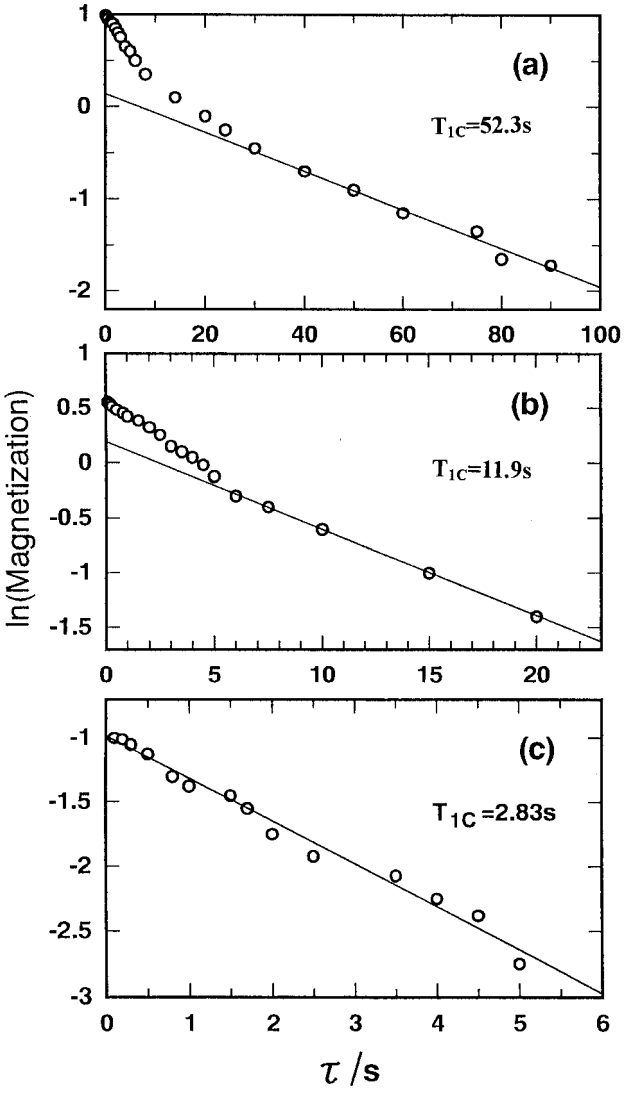

Fig. 15. Semi-logarithmic plot of the peak intensity of the resonance line of CH carbon II as a function of τ of the drawn PVA film ($\lambda = 10$) at 27–36°C.

for line III. To make clear this viewpoint, the total CP/MAS spectrum must be classified into the crystal and non-crystal components.

When the ^{13}C magnification $M_c(t)$ is observed by the CP technique, T_{CH}, the time constant for the energy exchange between ^{1}H and ^{13}C spin system, should be much shorter than $T_{1\rho C}$ and $T_{1\rho H}$ which are the spin–lattice relaxation times in their rotating frame. Accordingly, the ^{13}C magnification $M_c(t)$ may be approximated as follows:

$$M_c(t) = (M_e/T_{CH})\{1/T_{1\rho C} + 1/T_{CH} - 1/T_{1\rho H}\}^{-1} \times \{\exp(-t/T_{1\rho H}) - \exp(-t/T_{1\rho C} - t/T_{CH})\} \approx M_e\{\exp(-t/T_{1\rho H}) - \exp(-t/T_{CH})\} \quad (22)$$

Here M_e is the ^{13}C equilibrium magnetization obtained when both spin systems fully contact each other without any energy exchange with the lattice and therefore this value is proportional to the concentration of a given ^{13}C nucleus in a material. Eq. (22) means that $M_c(t)$ appears at the rate of the order of $(T_{CH})^{-1}$ and disappears at the rate of $(T_{1\rho C})^{-1}$.

Fig. 15 shows an example for the semi-logarithmic plot of the ^{13}C magnetization of the peak height of line II of the CH resonance line as a function of τ by T_1CP pulse sequence of Torchia [42] for the PVA film with $\lambda = 10$ measured at 27–36°C. The overall decay curve can be classified into three components by using a least-square method with a computer: (a) a slow decay curve; (b) an intermediate decay curve; and (c) a rapid decay curve. The initial slope of each decay curve yields T_{1C}. The overall decay curve measured for all the specimens used in this experiment can also classified into two or three components. These results are summarized in Table 2.

Fig. 16 shows an example for the CH_2 resonance line for PVA with $\lambda = 10$ measured at 27–36°C. The overall decay curve can be classified into three components as in the case of line II of the CH resonance. The overall decay curves in this experiment can also classified into two or three components. These results are also summarized in Table 2.

The overall decay curve classified into two or three components is thought to be due to the total contribution of crystalline and non-crystalline components. The longer T_{1C} value should indicate less mobility for components in the sample. If this is the case, the other one or two decay except the slower decay is related to the T_{1C} of non-crystalline component. To check this, T_{1C} measurements were also carried out by the standard saturation recovery method that is significant to estimate T_{1C} times shorter than a few seconds. The decay curves for the CH and CH_2 resonances showed one component. The results are listed in Table 3.

As listed in Table 2, the decay curve of line I of the CH resonance can be classified into two components. On the other hand, the decay curves of line II and III are classified into three components of T_{1C} at 27–36°C but the rapid decay disappeared at elevated temperature. For example, the disappearance occurred at 77–82°C for the undrawn specimen and at 99–104°C for the drawn specimen ($\lambda = 10$). This means that there exist two components in the non-crystalline region such as rubbery state and less disordered component. The two differences cannot be detected by X-ray diffraction. The less disordered component is thought to be located in the interfacial region between the crystalline and rubbery component. The disappearance of the shortest T_{1C} component at elevated temperature is due to the fact that the difference between the shortest and the intermidiate T_{1C} component is too small to be detected by T_1CP pulse sequence. That is, the molecular mobility of less ordered component is more active with increasing temperature and similar to that of rubbery state for the undrawn film. Actually, the two components could be detected for the drawn films with $\lambda = 10$ at 77–82°C, in spite of the disappearance

Table 2
^{13}C spin–lattice relaxation time of the respective carbons of undrawn and drawn PVA films measured at the indicated temperatures by T_1CP pulse sequence of Torchia

Sample	Temperature (°C)	CH								CH_2		
		Line I		Line II			Line III					
$\lambda = 1$	27–36	56.4	5.35	52.7	5.19	0.25	47.9	5.16	0.30	51.7	4.05	0.32
	77–82	12.3	0.97	15.1	0.72	–	17.6	0.57	–	18.9	0.58	–
	99–104	10.5	0.42	12.9	0.36	–	11.4	0.37	–	14.4	0.32	–
$\lambda = 10$	27–36	56.7	6.62	52.3	11.9	2.83	49.4	15.4	2.57	51.3	13.2	2.58
	77–82	24.1	1.55	23.9	5.10	0.20	29.3	4.35	0.50	26.9	5.54	0.64
	99–104	11.7	0.57	11.6	1.02	–	13.3	0.73	–	19.9	1.07	–

of the shortest T_{1C} component for the undrawn film. This probably is associated with the temperature concerning disappearance of the large dispersion peak of the loss modulus in Fig. 4; 70°C for the undrawn film and 100°C for the drawn film ($\lambda = 10$). Anyway, all the T_{1C} became shorter, reflecting more active chain mobility in the crystalline and non-crystalline phases with increasing temperature. The same tendency can be observed for the CH_2 resonance. To estimate the rapid decay, the T_{1C} values by the standard saturation recovery method are listed in Table 3. The results showed one decay for lines II and III of the CH resonance and the CH_2 resonance. The value at 27–36°C is not sensitive to draw ratio but the values measured at elevated temperatures are longer with draw ratio. At $\lambda = 1$, the value of T_{1C} corresponds to the longer time scale of the non-crystalline component estimated by T_1CP. At $\lambda = 10$, the value at 27–36°C is shorter than the corresponding value estimated by T_1CP while the value measured at 99–104°C is longer. Anyway, these results obviously demonstrated that the component with T_{1C} values of 46–57 s could be assigned to the crystalline component, while the other components correspond to the non-crystalline component. By using such differences in the T_{1C} values, we shall classify the CP/MAS spectra shown in Fig. 14 into the contribution of the crystalline and amorphous components.

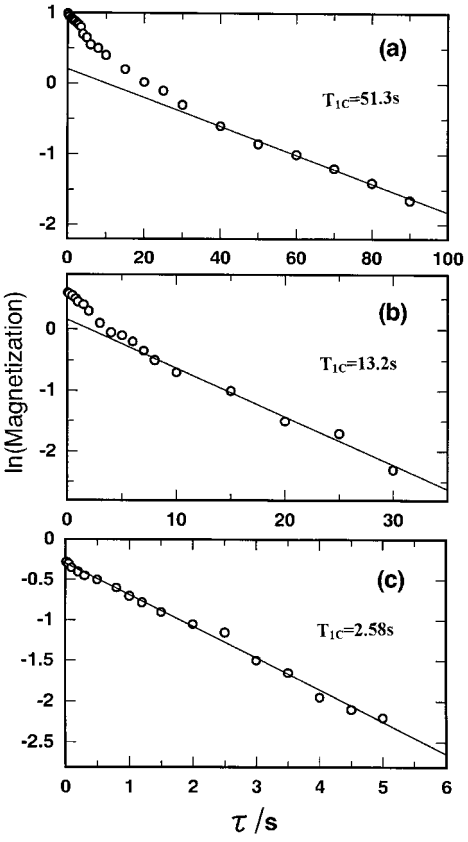

Fig. 16. Semi-logarithmic plot of the peak intensity of the resonance line of CH_2 as a function of τ of the drawn PVA film ($\lambda = 10$) at 27–36°C.

Incidentally, we must notice that T_{1C} is hardly affected by draw ratio. Such phenomenon as has been observed for polyethylene [43,44] has never been observed for PVA films prepared from Me_2SO or aqueous solutions [17]. For PVA specimens, the reverse relationship has been confirmed. Such an abnormal tendency reported already is thought to be due to unstable state of PVA crystallites. As listed in Table 3, the stable crystallites within specimens prepared from semi-dilute solution in Me_2SO and H_2O mixtures (60:40 composition) provide an interesting result that the longest T_{1C} component is independent of draw ratio.

Following Horii et al. [18], the T_{1C} values of the crystalline component are more than about 5 times larger than the values of the non-crystalline component. Using this difference in T_{1C}, the spectra of the two components are separately recorded. When resonance line j on a conventional CP/MAS spectrum contains the crystalline and non-crystalline components, the intensity M_j^{CP} may be expressed as a sum of the two contributions M_{jC} and M_{jNC}, as follows:

$$M_j^{CP} = M_{jC} + M_{jNC} \tag{23}$$

On the other hand, the intensity $M_j(t)$ of resonance line j measured at time t by the T_1CP pulse sequence may be given by:

$$M_j(t) = M_{jC}(0)\exp(-t/T_{1jC}) + M_{jNL}(0)\exp(-t/T_{1jNL}) + M_{jNS}(0)\exp(-t/T_{1jNS}) \tag{24}$$

Table 3
^{13}C spin–lattice relaxation time of the respective carbons of undrawn and drawn PVA films measured at the indicated temperatures by the saturation recovery method

Sample	Temperature (°C)	CH			CH_2
		Line I	Line II	Line III	
$\lambda = 1$	27–36	–	4.04	4.18	4.66
	77–82	–	0.50	0.48	0.58
	99–104	–	0.37	0.44	0.57
$\lambda = 10$	27–36	–	4.67	5.06	4.81
	77–82	–	3.39	4.17	2.99
	99–104	–	2.17	2.11	2.08

Here $M_{jC}(0)$, $M_{j\mathrm{NL}}(0)$ and $M_{j\mathrm{NS}}(0)$ are the intensities of the crystalline component and the non-crystalline components with the long and short T_{1C} values for resonance line j, respectively, and T_{1jC}, $T_{1j\mathrm{NL}}$ and $T_{1j\mathrm{NS}}$ are the ^{13}C spin–lattice relaxation times of the corresponding components. When the spectrum is measured by the T_1CP pulse sequence under the conditions $t \gg 5T_{1j\mathrm{NL}}$, it reflects the crystalline component with the intensities as a result of the disappearance of all the non-crystalline components. Therefore we have

$$M_{jC}(t) = M_{jC}(0)\exp(-t/T_{1jC}) \tag{25}$$

Fig. 17(b) shows the spectrum of the crystalline components measured at $t = 50$ s by using the undrawn film at 27–36°C. Since the T_{1C} values of the respective lines somewhat differ from each other, as shown in Table 2, the relative intensities of these lines are out of accord with those of the unrelaxed spectrum. The correlation of the relative intensities will be described later.

In addition to the method proposed by Hu et al. [17], the spectrum of the non-crystalline component can be obtained by subtracting the crystalline spectrum from the total CP/MAS spectrum. However, it is not simple, because the respective spectra of those components are completely superposed on each other. In doing so, we determined the values of $M_{jC}(0)$, $M_{j\mathrm{NL}}(0)$ and $M_{j\mathrm{NS}}(0)$ by the T_{1C} analysis shown in Fig. 14 and carried out the subtraction to obtain the following peak intensity of the crystalline and non-crystalline components for line II:

$$\frac{M_{jC}}{M_{jNC}} = \frac{M_{jC}(0)}{\{M_{j\mathrm{NL}}(0) + M_{j\mathrm{NS}}(0)\}} \tag{26}$$

The spectra thus obtained for the non-crystalline component is shown in Fig. 17(c). The correction of the exact relatively intensity of this spectrum will also be described later.

Fig. 18 shows the results of the computer lineshape analysis for the CH resonance line of the crystalline and non-crystalline components, respectively, at $\lambda = 1$ and Fig. 19 shows the results at $\lambda = 10$. Each line was assumed to be described as Gaussian. The composite curve of the three lines I, II and III, which is shown by a dotted line, is in good agreement with the experimental spectrum for both crystal and non-crystalline components. The integrated functions of lines I, II and III obtained by the analysis in Figs. 18 and 19 are given in Tables 4 and 5, together with their ^{13}C chemical shifts and linewidths. Here it may be noted that the fractions obtained from the spectra shown

Table 4
Integrated fractions, chemical shift and linewidth of line I, II and III for CH carbons of the crystalline spectra of undrawn and drawn PVA films measured at the indicated temperature

Sample	Temperature (°C)	Integrated fraction			Chemical shift (ppm)			Linewidth (ppm)		
		Line I	Line II	Line III	Line I	Line II	Line III	Line I	Line II	Line III
$\lambda = 1$	27–36									
	(observed)	0.088	0.452	0.460	77.6	71.6	65.1	1.95	2.02	2.15
	(corrected)	0.109	0.465	0.426						
	77–82									
	(observed)	0.114	0.485	0.401	77.1	71.6	65.1	1.84	1.91	2.01
	(corrected)	0.151	0.471	0.378						
	99–104									
	(observed)	0.149	0.487	0.364	77.1	71.6	65.2	1.96	1.85	1.95
	(corrected)	0.156	0.469	0.375						
$\lambda = 10$	27–36									
	(observed)	0.076	0.470	0.454	77.5	71.5	64.7	1.87	1.86	2.04
	(corrected)	0.114	0.494	0.392						
	77–82									
	(observed)	0.111	0.481	0.408	77.2	71.5	64.7	1.84	1.84	1.99
	(corrected)	0.163	0.543	0.294						
	99–104									
	(observed)	0.130	0.483	0.387	77.0	71.3	64.8	1.74	1.78	2.13
	(corrected)	0.190	0.475	0.335						

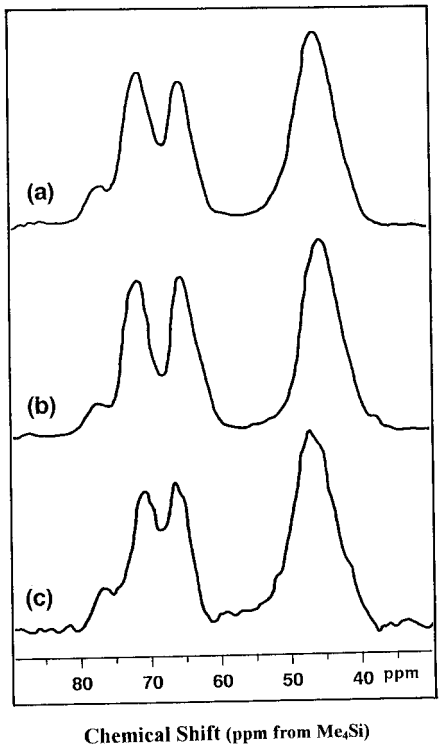

Fig. 17. ^{13}C CP/MAS spectra of the undrawn PVA films measured at 27–36°C: (a) total; (b) crystalline; (c) non-crystalline.

in Figs. 18 and 19 include the effect of the difference in T_{1C} among the CH carbons. As discussed before, the fractions of crystalline component were corrected according to Eq. (25) using T_{1C} values shown in Table 2. On the other hand, the correction of the fractions for the non-crystalline spectrum was made by multiplying the fraction of line j by factor g_j, which is expressed as:

$$g_j = \frac{M_j^{CP}}{(1+f_j)M_{jNC}(t)} \tag{27}$$

and then normalizing those values. Here M_j^{CP} and $M_{jNC}(t)$ are the peak intensities of line j for the spectra shown in Fig. 17(a) and (c), and f_j is the peak intensity ratio for the crystalline and non-crystalline components of line j, which is given by Eq. (26).

In Tables 4 and 5, the corrected fractions of the CH lines of the crystalline component are still in disaccord with the fraction of the triad tacticity of $mm : mr : rr = 0.23 : 0.50 : 0.27$. This is due to the fact that all OH groups in the *meso* sequences do not form intra-molecular hydrogen bonds and some of them are associated with the inter-molecular hydrogen bonding. In the measurement at 27–36°C, the mass fractions in Tables 4 and 5 suggest that the elongation causes a very slight increase in the number of intra-molecular hydrogen bonds in the crystalline and non-crystalline components. For example, the approximate fractions of line I indicate that intra-molecular and inter-molecular hydrogen bonds in the crystalline component are found at equal probability in the *meso* sequences, while in the non-crystalline component, the fraction of intra-molecular hydrogen bonds becomes close to 0.23. In addition to an increase in the relative intensity of line I, the relative intensity of line III decreased with draw ratio in both the components. This fact suggests that the inter-molecular hydrogen bonds may be broken by drawing and the intra-molecular hydrogen bonds are more preferably formed in the *mm* and *mr* sequences with draw ratio. Even so, it may be concluded that no

Table 5
Integrated fractions, chemical shift and linewidth of lineI, II and III for CH carbons of the non-crystalline spectra of undrawn and drawn PVA films measured at the indicated temperature

Sample	Temperature (°C)	Integrated fraction			Chemical shift (ppm)			Linewidth (ppm)		
		Line I	Line II	Line III	Line I	Line II	Line III	Line I	Line II	Line III
$\lambda = 1$	27–36									
	(observed)	0.142	0.441	0.417	76.7	71.1	66.1	2.02	2.11	1.88
	(corrected)	0.113	0.508	0.379						
	77–82									
	(observed)	0.130	0.541	0.329	77.0	71.5	65.5	1.76	2.00	2.15
	(corrected)	0.090	0.546	0.364						
	99–104									
	(observed)	0.118	0.464	0.418	75.6	70.9	65.4	1.98	1.91	2.11
	(corrected)	0.047	0.367	0.586						
$\lambda = 10$	27–36									
	(observed)	0.204	0.463	0.333	76.3	70.9	65.3	2.06	1.91	2.19
	(corrected)	0.183	0.460	0.357						
	77–82									
	(observed)	0.230	0.506	0.264	76.5	70.8	66.0	2.08	2.01	1.98
	(corrected)	0.126	0.566	0.308						
	99–104									
	(observed)	0.169	0.659	0.172	76.4	70.5	65.7	1.79	2.16	1.97
	(corrected)	0.159	0.651	0.190						

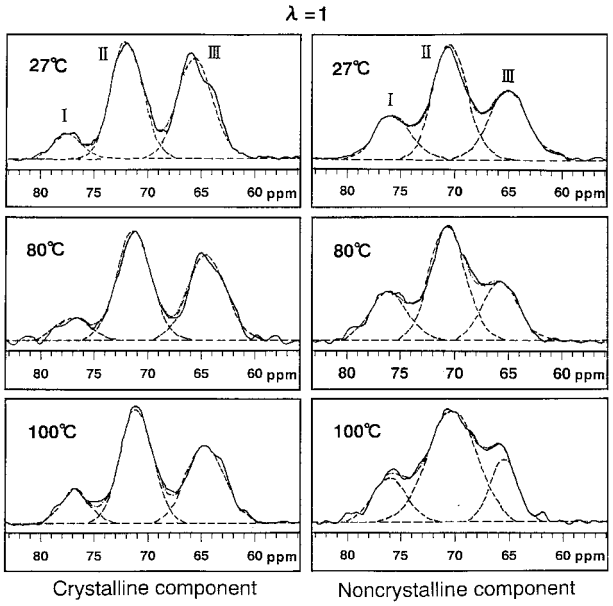

Fig. 18. Lineshape analysis for the CH line of CP/MAS spectra of the crystalline and non-crystalline components of the undrawn PVA film measured at the indicated temperature. The dotted line indicates the composite curve of the three components.

marked difference in the structure exists between the crystalline and non-crystalline regions, as judged from the hydrogen bonding in the triad sequences. Incidentally, the line widths and chemical shifts contain some ambiguous points because of the difficulty in conducting the complicated subtraction for the spectra discussed already.

According to the report by Hu et al. [17], the curve fitting for the films cast from aqueous or Me_2SO solutions could be

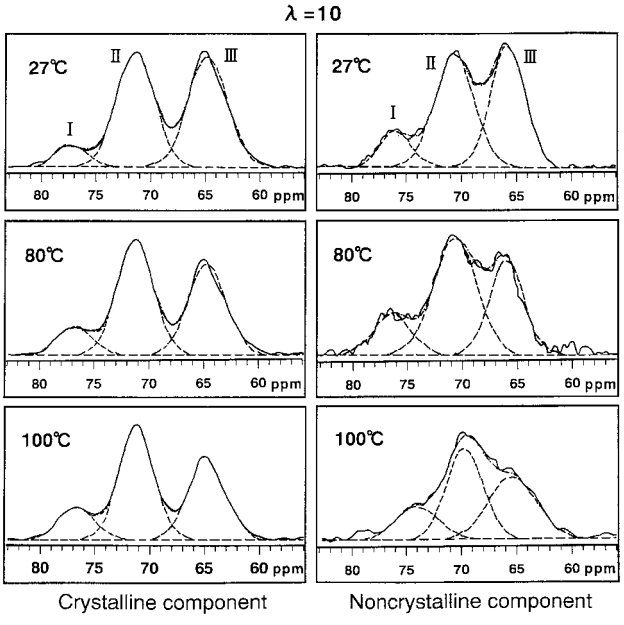

Fig. 19. Lineshape analysis for the CH line of CP/MAS spectra of the crystalline and non-crystalline components of the drawn PVA film $\lambda = 10$ measured at the indicated temperature. The dotted line indicates the composite curve of the three components.

achieved by introducing an additional peak detected as an upfield component of line III. They pointed out that line III_f of CH resonance in CP/MAS spectrum from crystalline phase is associated with the CH carbons which are chemically bonded OH group free from the intra- and inter-molecular hydrogen bonding as a result of the enhancement in molecular mobility by water. As for their dry films cast from aqueous or Me_2SO solutions, the fraction of OH groups free from hydrogen bonds in the non-crystalline component was found to be increased significantly with increasing draw ratio. This means that the PVA crystals become in less stable with increasing draw ratio and the corresponding crystal lattice modulus became lower with increasing temperature >120°C [16]. The unstable state causes the decrease in T_{1C} with draw ratio [17]. In the present films prepared by gelation/crystallization from the solutions in Me_2SO and H_2O mixtures with the 60:40 component, however, the crystal lattice modulus was maintained a constant value up to 170°C and decreased at 180°C as shown in Fig. 3. Of course, the spectra in Fig. 17 justifies the possibility of introduction of a very small component of III_f detected as an upfield component of line III. However, the component is much smaller than that reported by Hu et al. [17]. Such a very small composition can be obviously neglected as noise within an experimental error in order to avoid the arbitary of the peak separation.

To support the above analysis, the temperature dependence of crystallinity was measured by X-ray diffraction intensity as a function of s ($s = 2\pi \sin\theta_B/\lambda'$, where θ_B is the Bragg angle and λ' is the wavelength) for the undrawn film at the desired temperatures up to 200°C. The diffraction intensity from the crystal phase was obtained after the corrections similar to the method described in Section 2. Following Ruland [45–47] and Killian [48], the crystallinity for an undrawn film can be obtained as follows:

$$X_{cr} = X_{cr''}K \tag{28}$$

where $X_{cr''}$ and K are given by

$$X_{cr''} = \frac{\int_{s_0}^{s_p} s^2 I_{cr}(s)\,ds}{\int_{s_0}^{s_p} s^2 I(s)\,ds} \tag{29}$$

and

$$K = \frac{\int_{s_0}^{s_p} s^2\langle f^2\rangle\,ds}{\int_{s_0}^{s_p} s^2\langle f^2\rangle D_t^2\,ds}$$

where

$$\langle f^2\rangle = \frac{\sum n_j f_j^2}{\sum n_j} \tag{31}$$

$I_{cr}(s)$ and $I(s)$ in Eq. (29) are the intensity distributions from the crystal and the specimen, respectively. s_0 is the value

Table 6
Crystallinity (%) for the undrawn and drawn PVA films obtained by the Ruland methods

Integrated region (s_0–s_p)	Temperature (°C)												
	20		100		150		170		200		20	80	100
	$k=0$	$k=5.6$	$k=0$	$k=5.5$	$k=0$	$k=5.8$	$k=0$	$k=5.4$	$k=0$	$k=5.1$			
(A) An undrawn film													
0.058–0.396	14.3	21.0	13.1	20.3	13.3	21.1	13.9	21.4	14.3	21.5			
0.058–0.436	11.8	20.0	11.5	19.2	11.6	19.9	12.3	20.4	12.7	20.6			
0.058–0.556	9.70	20.8	9.86	20.9	9.19	20.2	9.76	20.4	10.3	20.9			
0.058–0.596	8.65	20.0	8.84	20.2	8.18	19.4	8.69	19.6	9.22	20			
0.058–0.636	7.83	19.6	8.08	19.9	7.39	19.0	7.86	19.1	8.39	19.5			
0.058–0.676	7.13	19.2	7.35	19.5	6.72	18.7	7.16	18.8	7.63	19.1			
average (%)		20.1		20		19.7		20		20.3			
(B) A drawn film ($\lambda = 10$)											31.6	30.4	32.1

associated with the initial scanning angle and s_p is related to the desired scanning angle for determining the crystallinity. f_j is the scattering factor of the jth atom and n_j is the number of atoms within a crystal unit. Therefore, $\langle f^2 \rangle$ means the average scattered intensity from the atoms. D_t is the coefficient containing the first- and second-order lattice distortion associated with thermal fluctuation, which is given by

$$D_t = \exp(-ks^2) \tag{32}$$

The temperature dependence of crystallinity which has been previously applied to polyethylene. The value of k must be determined to give a constant value of crystallinity which is independent of the integrated region ($s_0 - s_p$). Such a value was chosen by computer, instead of preparation of a monogram proposed by Ruland [45]. Unfortunately, the above method cannot be applied to the drawn films, since $I_{cr}(s)$ and $I(s)$ must be given as a function of θ_j like $I_{cr}(s, \theta_j)$ and $I(s, \theta_j)$, respectively. θ_j corresponds to the polar angle shown in Eq. (2). Because of an extremely long time experiments, the measurements for the drawn film at $\lambda = 10$ were done only at 10° interval from $\theta_j = 0$ to 90° in the range of 0.058–0.556 at 20, 80, and 100°C as an approximated method. The results are listed in Table 6. The results reveal that the crystallinity is independent of temperature up to 200°C. This tendency was quite different from the gradual decrease obtained for ultra-drawn polyethylene [19].

A series of the experimental results may be concluded that the crystallinity and the crystal lattice modulus as measured by X-ray diffraction are independent of temperature, and structure between crystal and non-crystal phases is not marked difference as measured by CP/MAS spectra. If these are the cases, drastic decrease in the storage modulus and the large dispersion at 20°C of the loss modulus in Fig. 4 are thought to be due to the fact that chain mobility of the amorphous (non-crystalline) phase becomes more promoted as temperature increases. Actually, the T_{1C} values decreased drastically with increasing temperature reflecting considerable mobility of molecular chains. In this paper, the elastic compliance of the amorphous (non-crystalline) phase was given as a function of intrinsic crystal and amorphous densities in Eqs. (20) and (21) to calculate Young's modulus in bulk. The two equations contain a big problem that the amorphous density is assumed to be a constant value independent of temperature and molecular orientational degree. At present, however, there is no way to calculate the temperature dependence of Young's modulus. To carry out the exact theoretical calculation of Young's modulus in bulk at elevated temperature, the amorphous density or rigidity must be represented as a function of temperature and molecular orientational degree. If the more quantitative information concerning molecular mobility in the crystalline and amorphous phases can be derived from ^{13}C NMR results, dramatic development shall be expected in the field of the mechanics of polymer materials at elevated temperature.

Recent investigation by Nakamae et al. [49] reported that the crystal lattice modulus of polyethylene measured at −155°C is almost equal to that at room temperature. If this is the case, the crystal lattice modulus takes a constant value from absolute temperature to its melting point. To study the reason, a lot of efforts must be done to measure the T_{1C} value of crystalline polymers such as PVA and polypropylene from absolute temperature to its melting point, in spite of extremely difficult. Anyway, it is certain that the exchange information between X-ray and ^{13}C NMR absolutely gives the clues to study the rigidity of polymer materials.

Finally, we shall discuss the different characteristics between polyethylene and PVA in terms of morphology, mechanical properties and molecular mobility, briefly. For ultra-drawn polyethylene films with $\lambda = 300$, it was concluded that the crystal lattice modulus is independent of temperature up to the melting point and the decrease in the storage modulus with temperature ascribes the decrease in the crystallinity [19]. In contrast, the crystallinities of

undrawn and drawn PVA films were confirmed to be almost constant up to 200°C. The longest T_{1C} values of the ultra-drawn polyethylene film were 3460 s at 27–40°C and 2400 s at 88–93°C, respectively, in the orthorhombic crystalline component, while they were 0.444 s at 27–40°C and 0.734 s at 88–93°C, respectively, in the non-crystalline component like a high-viscosity fluid rather than a solid state [44]. As discussed already for the PVA films in Table 2, the component with longest T_{1C} values of 46–57 s at 27–36°C can be assigned to be crystalline component and the other two or one components to be non-crystalline component. The T_{1C} values of both the components decreased drastically with increasing temperature indicating the drastic increase in molecular mobility. As discussed before, CP/MAS spectra offer the result that no marked difference in the structure exists between the crystalline and non-crystalline regions of the PVA films. This suggests that the crystallites of at-PVA are essentially less stable than those of polyethylene.

4. Conclusions

The morphology and mechanical properties of poly(vinyl alcohol) (PVA) were studied using PVA dry gel films which were prepared by crystallization from solutions in dimethyl sulfoxide (Me_2SO) and water (H_2O) mixtures. Me_2SO/H_2O composition was set to be 60:40. The hot homogenized solution was quenched by pouring it into an aluminum tray controlled at −80°C, thus generating a gel. The dry gel film could be stretched up to about 14-fold. The crystal lattice modulus measured by X-ray diffraction were 200–220 GPa, which was independent of temperature up to 170°C. However, the values became lower with further increase in temperature and the value at 200°C became 133 GPa. In spite of the temperature independence of the crystal modulus along the chain axis and of crystallinity, the storage modulus similar to Young's modulus decreases drastically with increasing temperature. The crystal strain along the *c*-axis showed a straight line against temperature. Such tendencies for the crystal lattice modulus and for the crystal strain against temperature indicated that the crystallites within the specimen used in these experiments are in more stable than those of the specimens reported before. To pursue the detailed relationship between mechanical property and molecular orientation, the orientational behavior of crystallites was estimated in terms of the orientation distribution function of crystallites, and then Young's modulus was calculated by using the generalized orientation factors of crystallites and amorphous (non-crystalline) chain segments calculated from the orientation functions of crystallites and amorphous chain segments. The actual theoretical calculation was carried out by using a three-dimensional model, in which the oriented crystalline layers are surrounded by an anisotropic amorphous phase and the strains of the two phases at the boundary are identical. The theoretical values were hardly affected by the composite mode of the crystalline and amorphous phases but they were in good agreement with the experimental ones. The ^{13}C NMR measurements suggested that the inter-molecular hydrogen bonds may be broken by drawing and the intra-molecular hydrogen bonds are more preferably formed in the *mm* and *mr* sequences with draw ratio. No marked difference in the structure, however, exists between the crystalline and non-crystalline regions, as judged from the hydrogen bonding in the triad sequences. Even so, T_{1C} values decreased drastically with increasing temperature reflecting more mobility of molecular chains. Accordingly, the drastic decrease in Young's modulus (storage modulus) is thought to be due to the fact that chain mobility in the amorphous phase becomes more pronounced as temperature increases. Since the crystallinity of PVA is much lower than that of polyethylene, the decrease of modulus in the amorphous phase with temperature causes significant effect on the decrease in Young's modulus in bulk.

Acknowledgements

We are indebted to Prof. Horii, Chemical Research Center Institute, Kyoto University, for his valuable comments on the ^{13}C NMR measurements and the analysis of the results.

References

[1] Smith P, Lemstra PJ. J Mater Sci 1990;15:505.
[2] Smith P, Lemstra PJ. J Mater Sci 1980;15:505.
[3] Smith P, Lemstra PJ, Pijpers JPL, Kiel AM. Colloid Polym Sci 1981;259:1070.
[4] Matsuo M, Inoue K, Abumiya N. Sen-i-Gakkaishi 1984;40:275.
[5] Matsuo M, Sawatari C. Macromolecules 1986;19:2036.
[6] Ogita T, Yamamoto R, Suzuki N, Ozaki F, Matsuo M. Polymer 1991;32:877.
[7] Sawatari C, Matsuo M. Macromolecules 1986;19:2726.
[8] Fukuhara K, Yokokawa T, Miyasaka K. J Polym Sci Polym, Phys Ed 1984;22:133.
[9] Kanamoto T, Tsuruta A, Tanaka K, Porter RS. Polym J 1983;15:327.
[10] Cha WI, Hyon SH, Ikada Y. J Polym Sci, Part B: Polym Phys 1994;32:297.
[11] Matsuo M, Kawase M, Sugiura N, Takamatsu S, Hara C. Macromolecules 1993;26:4461.
[12] Matsuo M, Sugiura N, Takamatsu S, Ogita T, Sakabe T, Nakamura R. Polymer 1997;38:5953.
[13] Rhodes M, Stein RS. J Polym Sci, Part A-2 1969;7:1539.
[14] Hibi S, Maeda M, Mizuno M, Nomura S, Kawai H. Sen-i-Gakkaishi 1973;29:79.
[15] Nomura S, Kawai H. J Polym Sci, Part A-2 1966;4:797.
[16] Nakamae K, Nishino T, Hata K, Matsumoto T. Kobunshi Ronbunshu 1986;43:133.
[17] Hu S, Horii F, Odani H, Narukawa H, Akiyama A, Kitamaru R. Kobunshi Ronbunshu 1992;49(4):361.
[18] Horii F, Hu S, Ito T, Odani H, Kitamaru R. Polymer 1992;33:2299.
[19] Matsuo M, Sawatari C. Macromolecules 1988;21:1658.
[20] Sakurada I, Nukushina K, Sone Y. Kobunshi Kagaku 1955;12:506.
[21] Xu C, Matsuo M. Macromolecules 1999;32:3006.
[22] Roe RJ, Krigbaum WR. J Chem Phys 1964;40:2608.

[23] Krigbaum WR, Roe RJ. J Chem Phys 1964;41:737.
[24] Roe RJ. J Appl Phys 1965;36:2024.
[25] Matsuo M, Sawatari C, Ohhata T. Macromolecules 1988;21:1317.
[26] Bin Y, Tanabe Y, Nakabayashi C, Kurosu H, Matsuo M. Polymer 2001;42:1183.
[27] Spendly W, Hext GR, Himsworth FR. Technometrics 1962;4:441.
[28] Matsuo M, Sato R, Yanagida N, Shimizu Y. Polymer 1992;33:1640.
[29] Nomura S, Matsuo M, Kawai H. J Polym Sci Polym, Phys Ed 1972;10:2489.
[30] Matsuo M, Hirota K, Fujita K, Kawai H. Macromolecules 1978;11:1000.
[31] Matsuo M, Xu C. Polymer 1997;38:4311.
[32] Matsuo M. Macromolecules 1990;23:326.
[33] Matsuo M, Sawatari C, Iwai Y, Ozaki F. Macromolecules 1990;23:3266.
[34] Gupta VB, Ward IM. J Macromol Sci 1967;B1:373.
[35] Maeda M, Hibi S, Itoh F, Nomura S, Kawaguchi T, Kawai H. J Polym Sci Polym, Phys Ed 1970;8:1303.
[36] Sawatari C, Matsuo M. Macromolecules 1986;19:2726.
[37] Tashiro K, Kobayashi M, Tadokoro H. Macromolecules 1978;11:914.
[38] Nomura S, Kawabata S, Kawai H, Yamaguchi Y, Fukushima A, Takahara H. J Polym Sci, A-2 1969;7:325.
[39] Terao T, Maeda S, Saika A. Macromolecules 1983;16:1535.
[40] Inoue Y, Chujo R, Nishioka A, Nozakura S, Iimuro H. Polym J 1973;4:244.
[41] Wu TK, Sheer ML. Macromolecules 1977;10:529.
[42] Torchia DA. J Magn Reson 1981;44:117.
[43] Zhu Q, Horii F, Tsuji M, Kitamura R. Nihon Reoroji-Kakkaishi 1989;17:35.
[44] Shimizu Y, Harashina Y, Sugiura Y, Matsuo M. Macromolecules 1995;28:6889.
[45] Ruland W. Acta Crystallogr 1960;13:1059.
[46] Ruland W. Acta Crystallogr 1961;14:1180.
[47] Ruland W. Polymer 1964;5:89.
[48] Killian HG. Kolloid Z Z Polym 1962;1:831.
[49] Nakamae K, Nishino T, Miyazaki H, International Conference on Advanced Fiber Materials, 1999.